A Modularized IPT With Magnetic Shielding for a Wide-Range Ubiquitous Wi-Power Zone

Eun S. Lee, *Student Member, IEEE*, Yeong H. Sohn, *Student Member, IEEE*, Byeong G. Choi, *Student Member, IEEE*, Seung H. Han, *Member, IEEE*, and Chun T. Rim, *Senior Member, IEEE*

***Abstract*—A wide-range ubiquitous wireless power environment, called a ubiquitous Wi-power zone, where any electric devices can be charged by three-dimensional (3-D)-omnidirectional wireless charging, is newly proposed in this paper. By virtue of the proposed direct-quadrature (DQ) transmitting (Tx) coils composed of multiple Tx modules with same size, a ubiquitous Wi-power zone having the transmitting (Tx) coils can be provided over wide-range 3-D space. In this area, a number of electric devices can be simultaneously charged during operation. Therefore, the proposed IPT is expected to be the next generation of wireless power transfer (WPT), as the internet of things (IoT), mobile devices, and sensor technologies evolve. For magnetic shielding behind the Tx coils and high power efficient operation of the proposed DQ Tx coils, providing an evenly distributed magnetic field, a conductive plate is adopted, and the effects of the conductive plate for the dipole coil structure were thoroughly evaluated by a 3-D FEM simulation. To create the proposed ubiquitous Wi-power zone, simulation-based optimum design procedures are established based on four design considerations and the optimized number of modularizations for the DQ Tx coils can be found by an optimum point of figure of merit (FoM). The DQ Tx module composed of the DQ Tx coils and series resonant capacitors was adopted as a standard unit of the proposed IPT so that different sizes and shapes of 3-D space can be utilized for universal use of the proposed ubiquitous IPT; hence, a general solution to create the proposed ubiquitous IPT is provided in this paper. A prototype 5 × 5 modularized IPT composed of 25 DQ Tx modules having the same size of 10 cm × 10 cm × 2 cm was fabricated and experimentally verified for a 1 m × 1 m × 0.7 m ubiquitous Wi-power zone. Experimental results showed that 95.5%, 92.1%, and 98.8% of high magnetic field uniformity for $z_1 = 25$ cm, 50 cm, and 75 cm, respectively, and 3-D omnidirectional wireless power delivery have been achieved; thus, meeting essential requirements for the proposed ubiquitous Wi-power zone. Nine Rx coils can be simultaneously charged with 14.2 W of total received load power and 8.2% power efficiency at $z_1 = 70$ cm.**

***Index Terms*—DQ rotating magnetic field, inductive power transfer (IPT), magnetic field uniformity, magnetic shielding, six degrees of freedom (6-DoF), three-dimensional (3-D) omnidirectional wireless charging, ubiquitous IPT, wi-power zone, wireless power transfer (WPT).**

I. Introduction

INTELLIGENT devices such as the Internet of Things (IoT), mobile devices, wearable devices, and smart sensors are rapidly evolving with the advent of the upcoming fourth industrial revolution. Such devices tend to have relatively large batteries and efforts are being made to reduce the device size [1]–[4]. Because multiple devices might be arbitrarily positioned in a confined three-dimensional (3-D) space and small-sized batteries should be used in the devices, the battery in each device should be frequently replaced, which wastes time and energy and induces high labor costs. Accordingly, an inherent solution involving compact battery size or a batteryless approach with continuous power delivery is required to solve these issues. Wireless power transfer (WPT) is a promising solution to deliver power to multiple devices [5]–[26]. As examples, radio frequency (RF) and infrared (IR) types of WPT systems may be used for long-distance wireless power delivery characteristics [5]–[8]. However, they have a limitation to simultaneously charge multiple devices due to a one-to-one wireless charging characteristic and cannot penetrate obstacles between transmitter (Tx) and receiver (Rx). In addition, precise control methods to align the Tx and Rx are required; hence, such RF and IR types of WPT have inherent limitations for these applications. On the other hand, inductive power transfer (IPT) may be a viable solution to simultaneously charge multiple electric devices [9]–[28]. The major applications for commercially available IPT products are currently limited to contact-type cases and less than 20 cm-off distance cases between Tx and Rx coils for mobile devices, drones, sensors, and electric vehicles [9]–[17]. Furthermore, existing WPT technologies are usually available with low degrees of freedom for wireless charging, and it is difficult to provide simultaneous wireless charging service for multiple Rx coils. This may impede application in the era of ubiquitous WPT such as the Wi-power zone described in this paper, where any small electric devices can be simultaneously charged with highest wireless charging freedoms during operation anytime

Manuscript received April 7, 2017; revised July 4, 2017, September 10, 2017, and November 18, 2017; accepted December 20, 2017. Date of publication January 3, 2018; date of current version August 7, 2018. This paper was presented at the International Future Energy Electronics Conference and ECCE Asia, Kaohsiung, Taiwan, June 3–7, 2017. This work was supported in part by the Commercializations Promotion Agency for R&D Outcomes funded by the Ministry of Science, ICT and Future Planning and in part by the Technology Innovation Program funded by the Ministry of Trade, Industry & Energy (MI, Korea) under Grant 20161210200740. Recommended for publication by Associate Editor O. Lucia. *(Corresponding author: Chun T. Rim.)*

E. S. Lee is with the Department of Nuclear and Quantum Engineering, Korea Advanced Institute of Science and Technology, Daejeon 34141, South Korea (e-mail: eunsoo86@kaist.ac.kr).

Y. H. Sohn and B. G. Choi are with the Department of Electrical Engineering, Korea Advanced Institute of Science and Technology, Daejeon 34141, South Korea (e-mail: sonyh216@kaist.ac.kr; choibk09@kaist.ac.kr).

S. H. Han is with TESLAS Co., Ltd., Daejeon 34051, South Korea (e-mail: hunplus@teslas.co.kr).

C. T. Rim is with School of Integrated Technology, Gwangju Institute of Science and Technology, Gwangju 61005, South Korea (e-mail: ctrim@gist.ac.kr).

Color versions of one or more of the figures in this paper are available online at http://ieeexplore.ieee.org.

Digital Object Identifier 10.1109/TPEL.2017.2789201

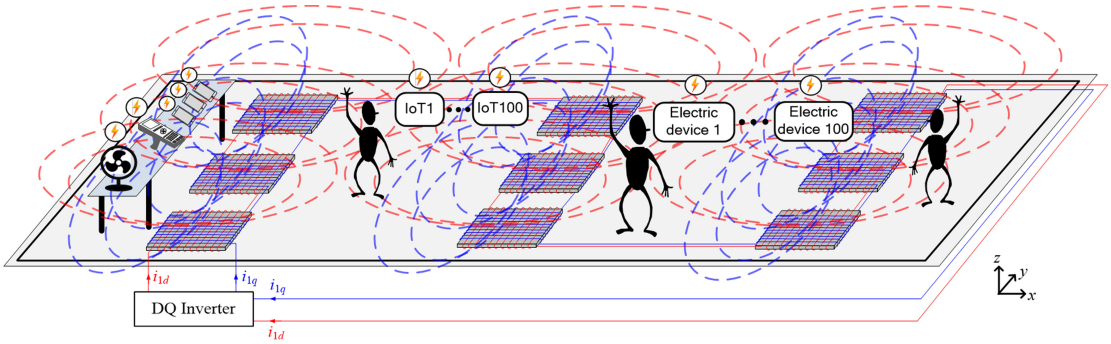

Fig. 1. Concept of the proposed ubiquitous Wi-power zone (3 × 3 modularization), where various electric devices including IoT sensors and electric devices are simultaneously charged with the highest degrees of freedom for wireless charging.

and anywhere, as shown in Fig. 1. Therefore, the following prerequisite conditions for the proposed ubiquitous Wi-power zone should be satisfied.

1) An evenly distributed magnetic field should be generated over wide-range 3-D space so that multiple electric devices equipped with Rx coils can be freely charged.
2) Electric devices should be charged, regardless of their arbitrary three-axes positions (x-, y-, and z-axes) and angles (roll, pitch, and yaw) for 3-D omnidirectional wireless charging, i.e., so-called six degrees of freedom (6-DoF) in this paper [9], [18]–[20].
3) The magnetic field generated from Tx coils should be shielded toward the opposite area of the Wi-power zone so that it is generated only to the wireless power service area.
4) The proposed WPT system should be easily manufactured with low cost and light weight with a minimal amount of cores.

From the second criterion, 6-DoF, which is the highest number of degrees of freedom for free-positioning wireless charging of Rx coils, should be guaranteed for the proposed ubiquitous Wi-power zone without volumetric structures of Tx and Rx coils. It has been identified that 6-DoF can be realized by 2-D plane-type of Tx and Rx coils, which provides the minimum physical dimension requirement for Tx and Rx coils, satisfying three arbitrary positions and angle rotations for wireless powering [9]. A direct and quadrature (DQ) rotating magnetic field over wide-range 3-D space generated by a plane Tx coil, which includes $\pi/2$ phase difference between two orthogonal Tx coil currents, is necessarily used for 6-DoF; hence, a plane Rx coil including vertical and horizontal coil windings is able to receive load power from either vertical or horizontal Rx coil winding [9]. From the third criterion, it is noteworthy that the magnetic field generated toward opposite side of the proposed Wi-power zone does not contribute wireless charging service. If the Tx coils are installed in each floors of the building, the magnetic field in the Wi-power zone may be distorted and mitigated due to phase difference between adjacent Tx coils installed in each floors unless the phase of all magnetic field is synchronized. Therefore, in this case, the receiving load power will be degraded without magnetic shield.

On the other hand, required installation places for the proposed ubiquitous Wi-power zone may be different regarding size and shape of 3-D space. In this case, DQ Tx coils designed only for the specific 3-D space should be manufactured, which cannot be utilized to the other 3-D space. Therefore, it is necessary to provide practical and general solutions for universal adoption of the proposed Wi-power zone to various installation places, regardless of size and shape of 3-D space.

In this paper, a wide-range Wi-power zone, which can provide an evenly distributed magnetic field over 3-D space, is newly proposed, as shown in Fig. 1. Two physically orthogonal-wound DQ Tx coils having orthogonal phase difference of DQ currents are adopted to generate a DQ rotating magnetic field. The modularized DQ Tx coils, which are used as a standard unit of the proposed IPT, are utilized so that the proposed ubiquitous Wi-power zone can be created in any size and shape of 3-D space; hence, the proposed Tx modules can be a general solution to provide the proposed ubiquitous Wi-power zone for universal adoption of the proposed IPT. To reduce core loss of the DQ Tx coils and mitigate the electromagnetic field (EMF) behind the proposed Tx coils without affecting the front side magnetic field, the conductive plate behind the proposed Tx coils is adopted for magnetic shielding and high power efficient operation. To create the proposed ubiquitous Wi-power zone in a confined 3-D space, an optimum baseline design procedure of the proposed modularized DQ Tx coils is established, considering four design considerations, and verified by a 3-D finite-element-method (FEM) simulation. An experimental prototype of the proposed DQ Tx coils targeting a 1 m × 1 m × 0.7 m ubiquitous Wi-power zone was fabricated by 5 × 5 modularization and verified by experiments.

II. Static Analysis of the Magnetic Shielding for Dipole Coil

A. Operating Principle of the Magnetic Shielding

It is important to select the most appropriate Tx coil structure to deliver wireless power over a long distance between Tx and Rx coils for the proposed ubiquitous IPT. There are typically two coil structures for various applications: the loop coils and dipole coils [9]–[27]. It has been identified that the dipole coil structure with ferrite core has higher magnetizing inductance by 60 times compared to that of a loop structure under all same size conditions [11]. Considering the fact that higher magnetizing inductance Lm results in higher induced voltage across

the Rx coil, the dipole coils are more preferred than the loop coils for long distance power delivery [9]–[11]. Thus, the dipole coil structure is adopted in this paper for the proposed DQ Tx coils while a 2-D plane-type coil structure is maintained. DQ currents in the steady state then have 90° phase differences to generate a DQ rotating magnetic field over a 3-D space and can be represented in phasor form as follows:

$$\boldsymbol{I}_d \equiv I_d \angle 0, \quad \boldsymbol{I}_q \equiv I_q \angle \frac{\pi}{2} = j\boldsymbol{I}_d \quad \because I_d = I_q. \tag{1}$$

From (1), magnetic flux density vectors generated by two orthogonal DQ Tx dipole coils $\boldsymbol{B}_{1d}$ and $\boldsymbol{B}_{1q}$ can be represented in a phasor form as follows:

$$\begin{aligned} \boldsymbol{B_{1d}} &\equiv (\boldsymbol{B}_{1dx}, \boldsymbol{B}_{1dy}, \boldsymbol{B}_{1dz}) = (B_{1dx}, 0, B_{1dz}) \\ \boldsymbol{B_{1q}} &\equiv (\boldsymbol{B}_{1qx}, \boldsymbol{B}_{1qy}, \boldsymbol{B}_{1qz}) = (0, jB_{1dy}, jB_{1dz}) \end{aligned} \tag{2}$$

where it is assumed in this paper that the D-axis Tx coil generates x- and z-axes magnetic field components and the Q-axis Tx coil generates y- and z-axes magnetic field components, considering the magnetic field generation characteristics of the dipole coil forward front and back sides [9]–[13].

When the Tx coil current passes through the dipole coil, the magnetic field is radiated from the dipole coil on every side [9]–[13]. The magnetic field generated from the dipole coil should be applied to the front side, which corresponds to the WPT area having Rx coils. On the other hand, a magnetic field should not be generated toward the back side, where no Rx coils are available, as shown in Fig. 2(a), where z_1 and z_2 lines are positioned at the center in the xy-plane, and the z_2 line starts from the magnetic shielding. Thus, magnetic shielding is adopted to suppress the EMF in this paper. As described in Fig. 2(b) for the operating principle of the magnetic shielding behind the Tx coils, the DQ magnetic field $\boldsymbol{\phi}_{1d}$ and $\boldsymbol{\phi}_{1q}$ generated from the DQ Tx coils can be mitigated by $\boldsymbol{\phi}_{cd}$ and $\boldsymbol{\phi}_{cq}$ generated from the canceling currents $\boldsymbol{I}_{cd}$ and $\boldsymbol{I}_{cq}$ on the magnetic shielding due to the 180° vector phase difference between the Tx coils and magnetic shielding for the magnetic field [27], [28]. By virtue of $\boldsymbol{\phi}_{cd}$ and $\boldsymbol{\phi}_{cq}$, besides EMF suppression toward the back side, the magnetic flux density inside the Tx core B_c can be reduced to a level lower than the saturation point of the ferrite core $\boldsymbol{B}_{sat}$ ($\boldsymbol{B}_c < \boldsymbol{B}_{sat} \approx 0.3$ T), as shown in Fig. 2(a); hence, the magnetic shielding improves the core loss of the DQ Tx core.

To evaluate the effects of the magnetic shielding adopted in the dipole coil, three major criteria are established in this paper: 1) the magnetic field at the front side w.r.t. z_1 for ubiquitous wireless power environment, 2) the magnetic field at the back side w.r.t. z_2 for magnetic shielding, and 3) core loss reduction in the Tx core for high power efficiency, as described in Fig. 2(a). As shown in Fig. 2(b), the total vector summation of the magnetic field at a specific point $\boldsymbol{B}_t$ determined by the magnetic field of the Tx coil and magnetic shielding $\boldsymbol{B}_1$ and $\boldsymbol{B}_c$ can be described from (2) as follows:

$$\begin{aligned} \boldsymbol{B_t} &= \boldsymbol{B_1} + \boldsymbol{B_c} = \boldsymbol{B_{1d}} + \boldsymbol{B_{1q}} + \boldsymbol{B_{cd}} + \boldsymbol{B_{cq}} \\ &= (B_{1dx} \pm B_{cdx})\boldsymbol{x_0} + (jB_{1qy} \pm jB_{cqy})\boldsymbol{y_0} + (B_{1dz} \\ &\quad \pm B_{cdz} + jB_{1qz} \pm jB_{cqz})\boldsymbol{z_0} \end{aligned} \tag{3}$$

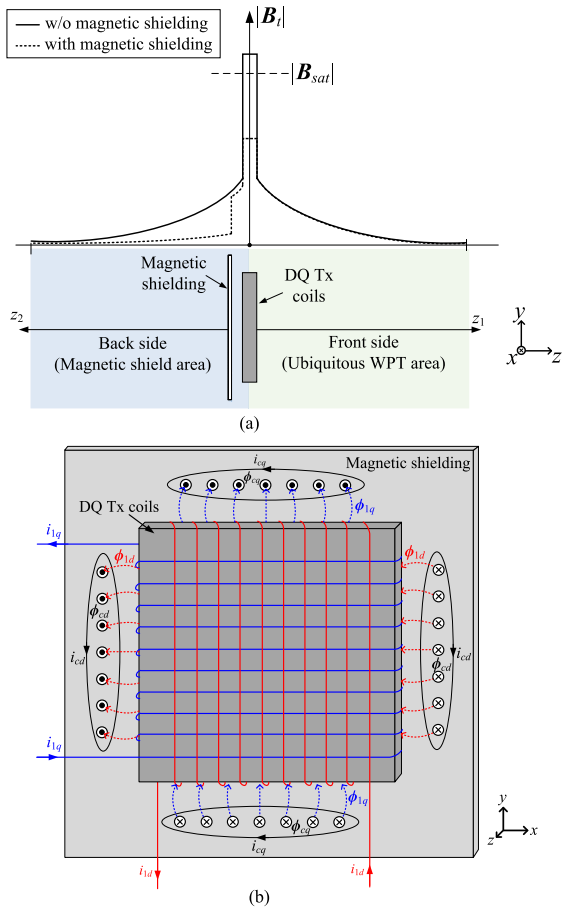

Fig. 2. Effect of magnetic shielding placed behind the proposed DQ Tx coils. (a) Side view. (b) Bird's view with magnetic field.

where x_0, y_0, and z_0 are unit vectors for x-, y-, and z-axes, respectively.

Then, the magnitude of $\boldsymbol{B}_t$ can be determined from (3) as shown in (4a)–(4c), at the bottom of the next page [9], [15], [24].

As identified from (4), the magnetic flux density generated by the Tx coil is enhanced toward the front side in (4b), whereas the magnetic flux density generated by the Tx coil is mitigated toward the back side in (4c). The magnitude of the total magnetic flux density B_t is eventually determined by $\boldsymbol{B}_{td}$ and $\boldsymbol{B}_{tq}$, which are vector summations by D- and Q-axes Tx coils and magnetic shielding, respectively.

As a third criterion, besides magnetic shielding, the magnetic field generated by the magnetic shielding $\boldsymbol{\phi}_{cd}$ and $\boldsymbol{\phi}_{cq}$ in Fig. 2(b) mitigates the magnitude of the magnetic field vector inside the Tx core B_c ($= |\boldsymbol{B}_c|$). Due to the use of a ferrite core in this DQ dipole coil, core loss of this dipole coil is inevitably generated, which is the major source of the total power loss in the Tx coil. Hysteresis loss, which accounts for the greatest portion of core loss, can be found in watt per unit volume by the following Steinmetz equation [10], [33], [34]:

$$\begin{aligned} P_{cv} &= C_m C_T f_s^p B_c^q [W/m^3] \\ \because C_T &= C_{T0} - C_{T1}T + C_{T2}T^2 \end{aligned} \tag{5}$$

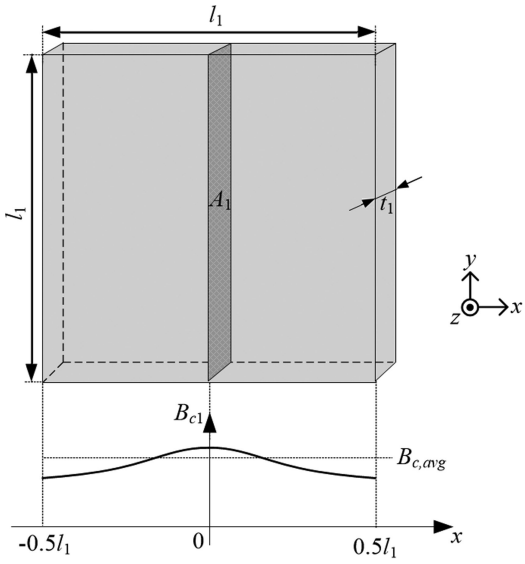

Fig. 3. Example of magnetic flux distribution of the dipole core.

where C_m and C_T are a core loss coefficient and a temperature correction parameter and f_s is the switching frequency.

As described in Fig. 3, the core loss can be calculated if the magnetic flux density B_{c1} is found and other parameters and coefficients, i.e., C_m, C_T, p, q, and f_s, are given. From (5), the core loss of the ferrite core in the Tx dipole coil can be quantitatively derived as follows:

$$P_{c1} = \int\int\int P_{cv}\,dxdydz = C_m C_T f_s^p \int_{-l_1/2}^{l_1/2} B_{c1}(x) A_1\,dx$$

$$\equiv C_m C_T f_s^p U_1 B_{c,avg} \tag{6a}$$

$$\because B_{c,avg} = \frac{1}{l_1}\int_{-l_1/2}^{l_1/2} B_{c1}(x)\,dx \tag{6b}$$

$$B_{c1} = \frac{1}{A_1}\int_{-t_1/2}^{t_1/2}\int_{-l_1/2}^{l_1/2} B_c^q(y,z)\,dydz \tag{6c}$$

$$U_1 = l_1 A_1 = l_1^2 t_1 [m^3] \tag{6d}$$

where U_1 is the total volume of the ferrite core used in the proposed DQ Tx coils. Note that $B_{c,avg}$ is proportional to the core loss of the Tx coils P_{c1} if the other parameter values of C_m, C_T, p, f_s, and U_1 are fixed.

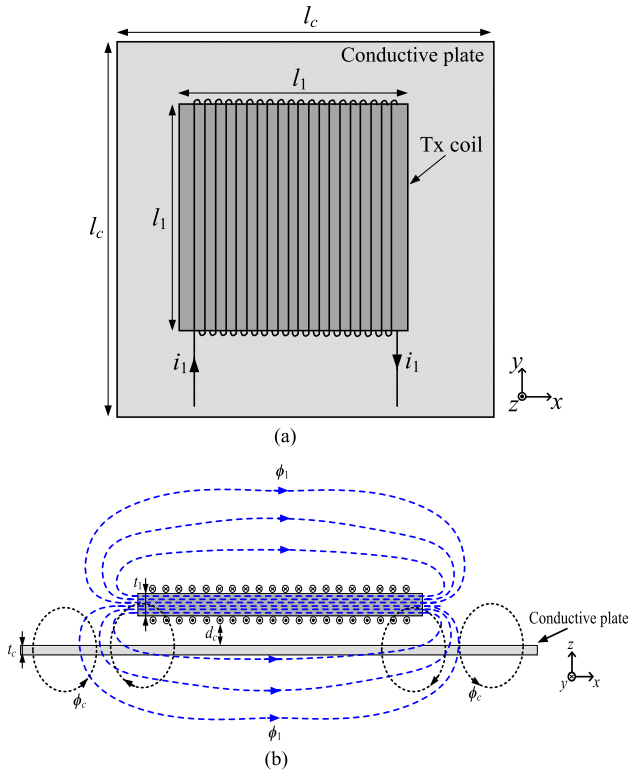

Fig. 4. Configuration of the Tx coil with a conductive plate. (a) Front view. (b) Side view with magnetic field.

B. Conductive Plate for the Magnetic Shielding

As one of the magnetic shielding methods, large ferrite core tile can be used behind the Tx coils. However, due to its large amount of ferrite cores, heavy, and high cost, such ferrite tile is not considered throughout this paper. Instead, a conductive plate having high conductivity, light weight, and low cost is adopted throughout this paper, as shown in Fig. 4, where l_c and t_c are the length and thickness of the conductive plate and l_1, t_1, and i_1 are the length, thickness, and current of the Tx coil. In this section, only a one-axis wound dipole coil is considered for simplicity of analysis and an aluminum plate is selected as the conductive plate. As shown in Fig. 4(b), when the conductive plate is adopted behind the dipole coil driven by i_1, eddy currents on the magnetic shielding caused by ϕ_1 generate ϕ_c, which is 180° phase shifted compared to ϕ_1. By this principle, the magnetic field ϕ_1 inside the Tx core and at the back side is mitigated by ϕ_c.

$$B_t \equiv |\boldsymbol{B_t}| = |\boldsymbol{B_1} + \boldsymbol{B_c}| = \sqrt{|B_{1dx} \pm B_{cdx}|^2 + |jB_{1qy} \pm jB_{cdy}|^2 + |B_{1dz} \pm B_{cdz} + jB_{1qz} \pm jB_{cqz}|^2}$$

$$= \sqrt{|B_{1dx} \pm B_{cdx}|^2 + |B_{1qy} \pm B_{cqy}|^2 + |B_{1dz} \pm B_{cdz}|^2 + |B_{1qz} \pm B_{cqz}|^2} \equiv \sqrt{{B_{tdx}}^2 + {B_{tdz}}^2 + {B_{tqy}}^2 + {B_{tqz}}^2}$$

$$\equiv \sqrt{|\boldsymbol{B}_{td}|^2 + |\boldsymbol{B}_{tq}|^2} \tag{4a}$$

$$\because B_{tdx} = B_{1dx} + B_{cdx}, \quad B_{tdz} = B_{1dz} + B_{cdz}, B_{tqy} = B_{1qy} + B_{cqy}, \quad B_{yqz} = B_{1qz} + B_{cqz} \quad \text{for front side} \tag{4b}$$

$$B_{tdx} = B_{1dx} - B_{cdx}, \quad B_{tdz} = B_{1dz} - B_{cdz}, B_{tqy} = B_{1qy} - B_{cqy}, \quad B_{yqz} = B_{1qz} - B_{cqz} \quad \text{for back side.} \tag{4c}$$

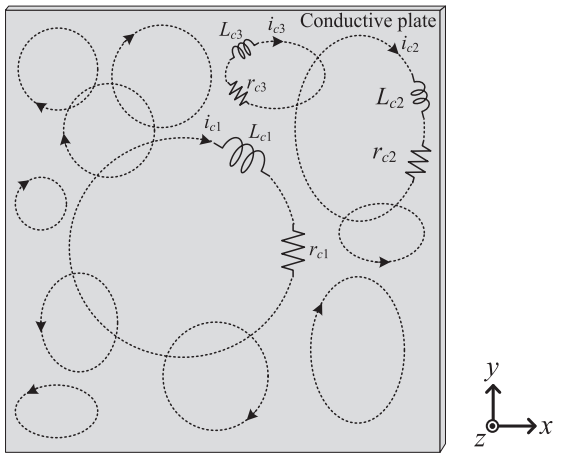

Fig. 5. Qualitative behavior of the conductive plate when an external magnetic field is applied to it.

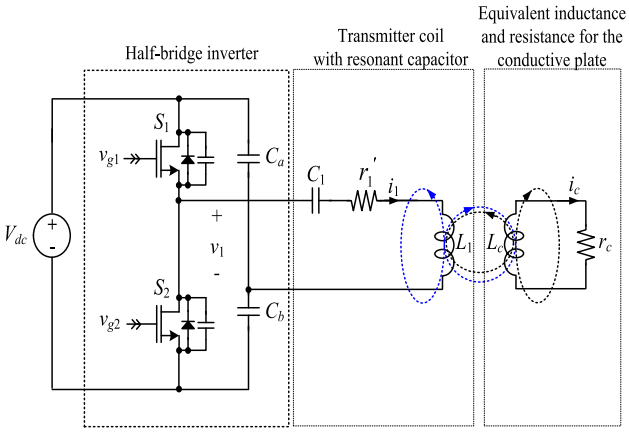

Fig. 6. Circuit diagram of the proposed IPT coupled with the conductive plate, assuming that the coupling effect of Rx coils is neglected due to the loosely coupled IPT.

As shown in Fig. 5, arbitrary several eddy current loops generated by ϕ_1 may be composed of $L_{c1}\&r_{c1}, L_{c2}\&r_{c2}, L_{c3}\&r_{c3}$, etc. In this case, such eddy currents, e.g., i_{c1}, i_{c2}, and i_{c3}, are generated through each inductance and resistance path. Because the effect of the conductive plate cannot be theoretically analyzed by explicit circuit modeling, the total equivalent self-inductance and internal resistance of the conductive plate are modeled as L_c and r_c to simply identify the qualitative behavior of the conductive plate, as shown in Fig. 6, where the Tx coil current I_1 is driven by a half-bridge inverter and the coupling effect between the Tx and Rx coils is neglected due to the loosely magnetic coupling. In Fig. 6, L_1 and L_c are modeled for self-inductance of the Tx coil and the conductive plate, respectively, and C_1 is a series resonant capacitor. Throughout this paper, it is assumed that the total equivalent resistance including the core loss of the ferrite core, the copper loss of the Tx coils, and the equivalent series resistance (ESR) of the resonant capacitor can be represented as a series-connected resistance when the inductance and capacitance resonate in series [10], [11], [23], [27]; hence, the total equivalent resistance of the Tx coil composed of L_1 and C_1 can be represented as

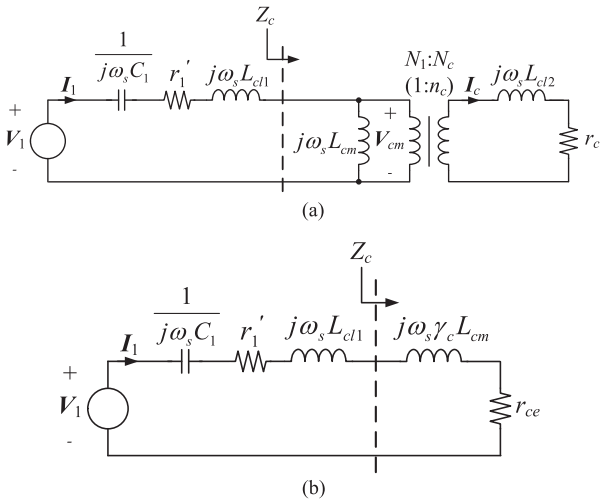

Fig. 7. Simplified circuit of the proposed IPT with magnetic shielding, where fundamental components of voltage and current are considered only. (a) Equivalent static circuit of Fig. 6. (b) Simplified static circuit of (a), reflected to primary side.

r_1. If the conductive plate is adjacent to Tx dipole coil, then r_1 is changed to r_1', as shown in Fig. 6. In this case, r_1' is smaller than $r_1\,(r_1' r_1)$ due to the core loss reduction by the conductive plate, as identified from Fig. 4, which will be verified in Section IV.

In this section, the steady-state behaviors of the circuit in Fig. 6 are analyzed by neglecting high-order switching harmonics, and parasitic components associated with circuit elements are neglected for simplicity of analysis. Fundamental components of voltage and current of the circuit in Fig. 6 are considered only. Then, a simplified static circuit of the proposed IPT with the conductive plate can be represented, as shown in Fig. 7, where L_{cm} and n_c are modeled for the magnetizing inductance and the turn ratio between the Tx coil and the conductive plate, respectively, as follows:

$$L_1 \equiv L_{cm} + L_{cl1}, \quad L_c \equiv n_c^2 L_{cm} + L_{cl2} \tag{7}$$

where L_{cl1} and L_{cl2} are leakage inductance.

To identify variations of the equivalent inductance and resistance w.r.t. the existence of the conductive plate, an impedance seen from primary side Z_c is derived as follows:

$$Z_c = j\omega_s L_{cm} // \frac{(j\omega_s L_{cm} + r_c)}{n_c^2} = j\omega_s L_{cm}\gamma_c + r_{ce} \tag{8a}$$

$$\gamma_c \equiv \frac{r_c^2 + \omega_s^2 L_{cl2} L_c}{r_c^2 + \omega_s^2 L_c^2} \approx \frac{L_{cl2}}{L_c} < 1, r_{ce} \equiv \frac{n_c^2 \omega_s^2 L_{cm}^2 r_c}{r_c^2 + \omega_s^2 L_c^2}$$

$$\approx \frac{n_c^2 L_{cm}^2 r_c}{L_c^2} > 0 \quad (\because r_c \ll \omega_s L_c)\,. \tag{8b}$$

As identified from (8), the inductance of the Tx coil after the conductive plate is adjacent to the Tx coil decreases because $\gamma_c < 1$. On the other hand, the total equivalent resistance of the Tx coil by the conductive plate becomes $r_1' + r_{ce}$, where r_1' and r_{ce} are the internal resistance of the Tx coil including core and copper losses and the eddy loss term of the conductive plate, respectively. In general, $r_1' + r_{ce}$ may be considered to be larger

than r_1 due to adding the eddy current loss caused by the conductive plate. In this dipole coil case, however, it is noteworthy that $r_1 > r_1' + r_{ce}$, although $r_{ce} > 0$. This is because core loss of the Tx coil can be significantly reduced by eddy current generated from the conductive plate, which has greater influence on the total loss than the eddy current loss in the conductive plate. This theoretical conclusion by the proposed equivalent circuit modeling of the IPT in Figs. 5–7 will be verified in Section IV.

To identify the behavior of magnetic shielding behind the conductive plate, induced voltage in the conductive plate V_{co} in Fig. 7 can be derived by Faraday's law as follows:

$$v_{co}(t) \equiv n_c v_{cm}(t) = -N_c \frac{d\varphi_1(t)}{dt}$$
$$\rightarrow \quad \boldsymbol{V}_{co} = -j\omega_s N_c \boldsymbol{\phi}_1 \quad (\because \boldsymbol{\phi}_1 \propto \boldsymbol{I}_1). \tag{9}$$

From (9), the equivalent eddy current $\boldsymbol{I}_c$ in Fig. 7(a) can be expressed as follows:

$$\boldsymbol{I}_c = \frac{\boldsymbol{V}_{co}}{r_c + j\omega_s L_c} = \frac{-j\omega_s N_c \boldsymbol{\phi}_1}{r_c + j\omega_s L_c} \cong \frac{-N_c \boldsymbol{\phi}_1}{L_c} \tag{10a}$$
$$\therefore \boldsymbol{I}_c \propto \boldsymbol{\phi}_c \propto -\boldsymbol{\phi}_1. \tag{10b}$$

As identified from (10), the phase difference of the magnetic field between the Tx coil and the conductive plate becomes 180°, which mitigates $\boldsymbol{\phi}_1$ for core loss reduction and magnetic shielding.

C. Simulation Verification of the Conductive Plate

As identified from (4) and (6), B_t and B_c should be analyzed to investigate the magnetic field characteristics by magnetic shielding applied to the DQ Tx dipole coils. For various applications, a conductive plate is generally used as magnetic shielding, i.e., IPT, building, magnetic shielded rooms, and medical instruments [27]–[32]. Effects of the conductive plate have been analyzed by an assumed certain eddy current loop model [29], [30]. However, this model is only valid when an equally distributed magnetic field is applied by a perpendicular magnetic field; hence, effects of the conductive plate are inherently not accurate due to the surrounding environment, skin effects of the conductive plate, and a nonequally applied magnetic field toward the conductive plate for IPT applications. The conductive plate is generally used to shield the EMF for WPT [27], [28]. In this paper, a conductive plate is applied to DQ Tx coils for magnetic shielding and coreless reduction, as identified from Figs. 2 and 3. Unfortunately, it is not possible to theoretically analyze the effect of magnetic shielding because the complicated magnetic field generated from the Tx dipole coil is distorted by the ferromagnetic core and static circuit modeling of eddy current loops and its parameter values of L_c and r_c in Figs. 5–7 cannot be quantitatively derived for the conductive material. Therefore, simulation-based verification for the magnetic shielding is inevitably adopted in this paper.

To verify three major criteria, as identified from the previous section, FEM simulations by ANSYS 3D Maxwell simulation tool were performed. For the simulation verification, the parameters in Fig. 4 were chosen as an example: $l_1 = 100$ mm, $I_1 = 1$ A, $N_1 = 20$ turns, $t_1 = 5$ mm, and $t_c = 1$ mm. The other parameters that influence the effect of the magnetic shielding are the length of the conductive plate l_c and the distance between the Tx coil and the conductive plate d_c. The magnetic field B_t in the front and back sides was found w.r.t. z_1 and z_2 lines, as shown in Fig. 2(a), and the core loss of the Tx core can be found by B_{c1} in Fig. 3 and by calculating $B_{c,avg}$ from (6). As shown in Fig. 8, the front side magnetic field B_t is exponentially decreased w.r.t. z_1 and shows little difference, even though various l_c and d_c cases are evaluated. This implies that the magnetic field generated from the conductive plate ϕ_c cannot reach the front side of the Tx dipole coil. On the other hand, $B_{c,avg}$, which is proportional to the core loss of the Tx coil P_{c1} in (6a), decreases when l_c increases and d_c decreases, as shown in Fig. 9. The smaller d_c makes a large V_{co} in (9) and (10), which may increase ϕ_c. When l_c becomes large, a large ϕ_c may be generated due to expanded eddy current loops. Note that $B_{c,avg}$ no longer decreases if $l_c > 5.0l_1$.

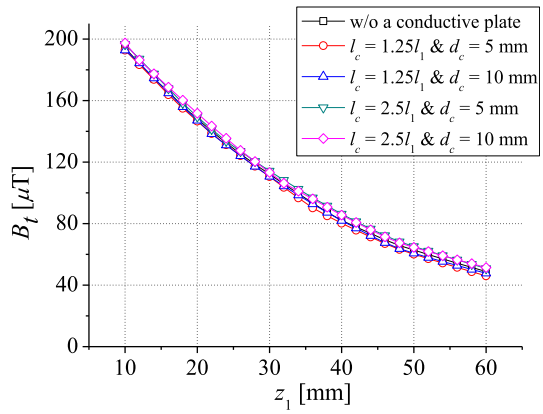

Fig. 8. Simulation results of B_t w.r.t. z_1.

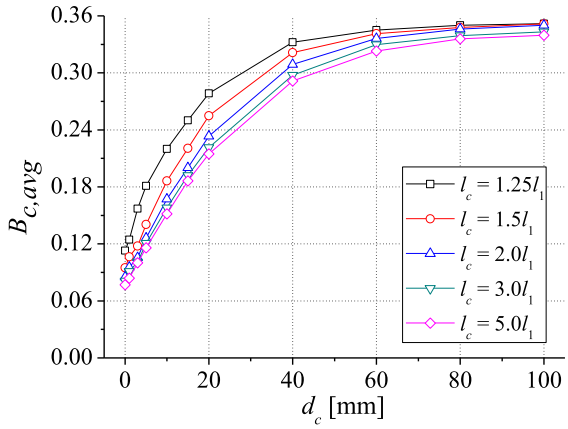

Fig. 9. Simulation results of $B_{c,avg}$ for various d_c and l_c.

To investigate the effect of the magnetic shield behind the Tx coil, B_m, the averaged value of the magnetic flux density at the xy-plane, corresponding to $l_1 \times l_1$ of the plane area, w.r.t. z_2 in Fig. 2(b), is defined in this paper as follows:

$$B_m(z_2) \equiv \frac{1}{N_x N_y} \sum_{a=1}^{N_y} \sum_{b=1}^{N_x} B_{t,ab} \tag{11}$$

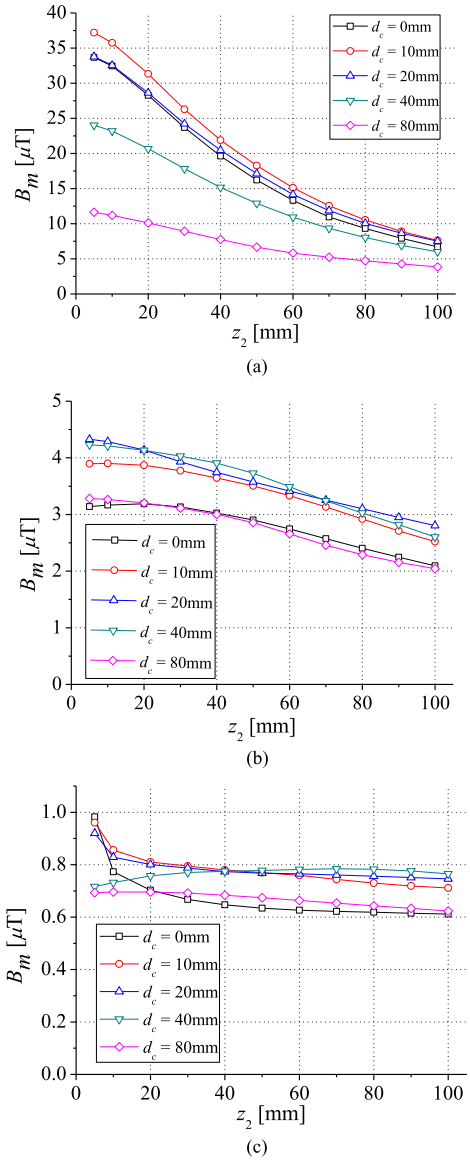

Fig. 10. Simulation results of B_m for magnetic shield behind the Tx coil. (a) $l_c = 1.25l_1$. (b) $l_c = 2.5l_1$. (c) $l_c = 5.0l_1$.

where N_x and N_y are sampling points at the xy-plane and it is assumed that $N_x = N_y = 100$ in this paper for simulation verification.

As shown in Fig. 10, when l_c increases, the effect of the magnetic shield becomes significant due to the expanded eddy current loops for a large ϕ_c. Note that B_m no longer decreases if $l_c > 5.0l_1$, although not shown in this paper. On the other hand, when d_c increases, B_m increases and decreases. As shown in Figs. 10(a)–(b), when the conductive plate is very close to the Tx coils, i.e., $0 < d_c < 15$ mm for $l_c = 1.25l_1$ and $0 < d_c < 30$ mm for $l_c = 2.5l_1$, the eddy current I_c may become large from (10a) due to the small distance d_c between the Tx coil and the conductive plate, which largely mitigates ϕ_1 at the back side. When d_c increases further, i.e., $d_c > 15$ mm for $l_c = 1.25l_1$ and $d_c > 30$ mm for $l_c = 2.5l_1$, B_m decreases because I_c becomes smaller and the distance from the Tx coil to z_2 point increases. Therefore, as identified from Figs. 8–10, it is found that the effect of the conductive plate becomes larger when larger l_c and smaller d_c are adopted in terms of $B_{c,avg}$ and B_m.

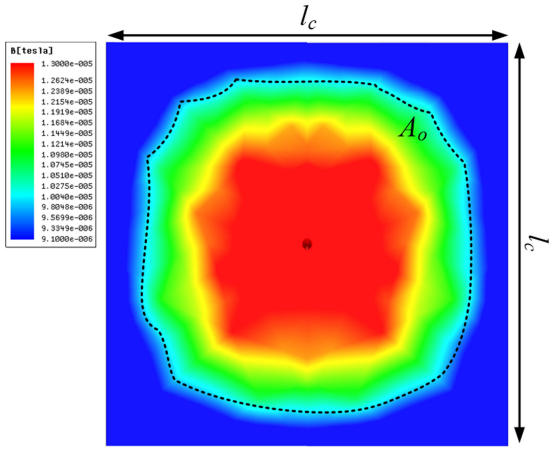

Fig. 11. FEM simulation result of the magnetic field distribution at $z_1 = 0.5l_c$ for 1×1 DQ Tx coil.

III. Modularization of the Proposed DQ Tx Coils

A. Optimum Baseline Design for DQ Tx Coil Modularization

To create the proposed ubiquitous Wi-power zone for a given 3-D space, several design criteria should be carefully considered to complete the baseline design of the proposed DQ Tx coils. As introduced in Section I for the prerequisite conditions of the proposed ubiquitous IPT, the following four design criteria are introduced in this paper in order to find an optimum solution.

1) *Magnetic field uniformity $U_B(z_1)$:* This is the proportion of the total area ($A_t = l_c \times l_c$) to occupied area A_o having a maximum magnetic flux density value over -3 dB ($= 70.7\%$) at the xy-plane w.r.t. z_1, as described in Fig. 11. U_B indicates how the magnetic field is evenly distributed over 3-D space. Thus, U_B is defined as $A_o/A_t \times 100$ [%] in this paper. The higher value implies higher uniformity for magnetic field distribution.
2) *Magnetic shielding $B_m(z_2)$:* A lower value of B_m implies higher capability of the magnetic shield, as identified from (11).
3) *Core loss of the Tx coils P_{c1}:* Lower core loss of all Tx cores implies higher power efficiency.
4) *The amount of ferromagnetic core M_1 that is used:* This factor determines the cost and weight of the proposed IPT system for installation. The lower value implies lower cost and lighter weight.

For magnetic field generation over 3-D space, a DQ Tx dipole coil with size of the ubiquitous Wi-power area may be installed, as shown in Fig. 12(a). On the other hand, the DQ Tx coil can be divided into several modules under the given installation space, as shown in Fig. 12(b)–(c). Therefore, the proposed DQ Tx coils should be designed in terms of modularization, considering the four design criteria.

As one of example to illustrate the design procedure of the proposed DQ Tx coils, it is assumed that the installation space

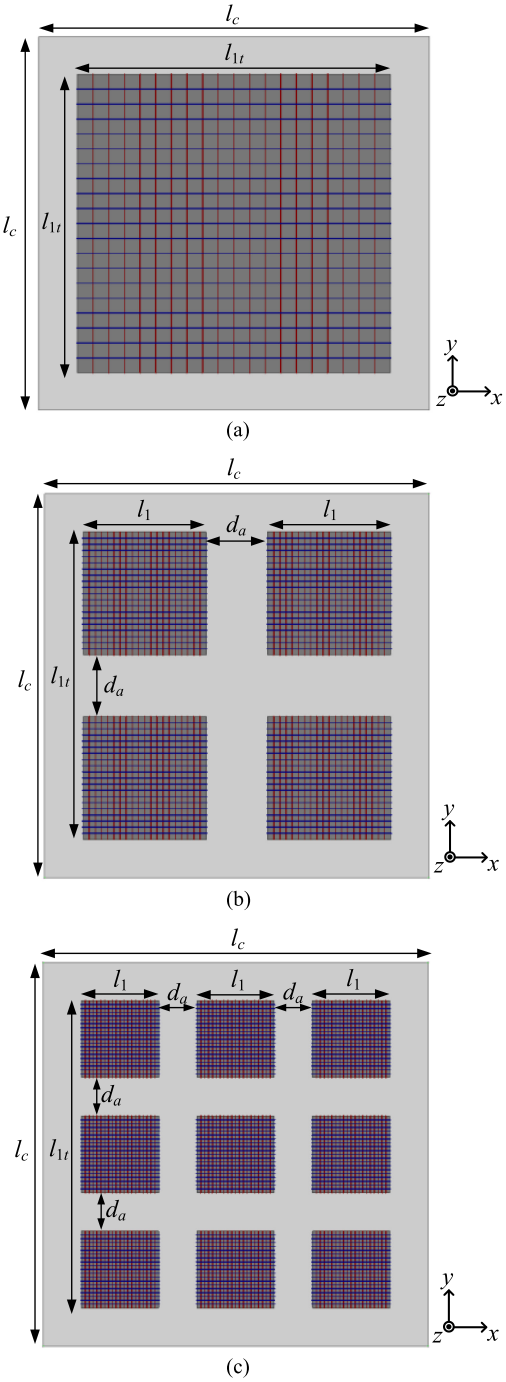

Fig. 12. Simulation schemes of the proposed modularized DQ Tx coils. (a) 1×1 case. (b) 2×2 case. (c) 3×3 case.

is given as 1 m $\times$ 1 m : $l_c = 1$ m and $t_c = 1$ mm in this section. For the magnetic shield, various conductive materials, e.g., aluminum, copper, and iron, can be selected: an aluminum plate is adopted behind the Tx coils throughout this paper due to its high conductivity, reasonable price, and light weight. According to FEM simulation results, there was little difference between aluminum plates and the other conductive materials, which are not included in this paper due to its similar characteristics and limited pages. The thickness of the ferrite core in the DQ Tx coils t_1 is selected as 16 mm, considering core saturation of the ferrite core. The number of DQ windings is 20 turns, and l_{1t} is fixed to 80 cm, i.e., $l_c = 1.25 l_{1t}$, as identified from Figs. 8–10. Assuming that the distance between DQ Tx coils d_a is half of l_1 as one of the design examples, the length of the DQ coil unit l_1 is then determined as follows:

$$l_{1t} = N_m l_1 + (N_m - 1) d_a \rightarrow l_1 = \frac{l_{1t}}{1.5 N_m - 0.5} (\because d_a = 0.5 l_1) \quad (12)$$

where N_m is the number of modularizations.

It is assumed that the goal of the proposed design procedure is to deliver the same maximum value of the magnetic field at the same distance condition: hence, DQ currents for each N_m cases are set in order to satisfy $B_t|_{z1=75\text{ cm}} = 6.0\ \mu$T, which can be found by a FEM simulation. From these design assumptions, the length of the DQ Tx module l_1 and the DQ current of the Tx coils I_{1d} and I_{1q} are summarized in Table I.

The magnetic field uniformity U_B has a different tendency for various N_m and z_1, as shown in Fig. 13, where only five cases are presented as examples. It can be found that the average value of the magnetic field uniformity for 10 cm $< z_1 <$ 100 cm $U_{B,avg}$ is quite low over a distance of 20 cm $< z_1 <$ 100 cm when $N_m = 1$, which means the use of only one DQ Tx coil in Fig. 12(a) may not be recommended for high magnetic field uniformity over 3-D space. B_m, which represents the magnetic shield effect behind the Tx coils, decreases when the distance z_2 increases, as shown in Fig. 14. The average values of B_m for 20 mm $< z_2 <$ 600 mm for all cases $B_{m,avg}$ are quite similar even when N_m changes. The 1×1 modularization case has a relatively lower value compared to the other cases due to the small value of DQ Tx coils, as identified from Table I.

Four criteria for the baseline design of the proposed IPT have been established when long distance wireless power delivery is guaranteed. To select the most appropriate number of modularization N_m, considering the four criteria, as introduced in this section, the following figure of merit (FoM) is defined for the baseline design procedure of the proposed IPT in this paper

$$FoM \equiv (1 - 0.01 U_{B,avg}) \times B_{m,avg} \times P_{c1,nom} \times M_{1,nom}. \quad (13)$$

In (13), $U_{B,avg}$ is the averaged value of the magnetic field uniformity for 10 cm $< z_1 <$ 100 cm and $B_{m,avg}$ is the average value of the magnetic field for 20 mm $< z_2 <$ 600 mm. $P_{c1,nom}$ and $M_{1,nom}$ are normalized values of the total core loss and the weight of the proposed Tx coils, respectively. A lower value of the FoM in (13) is recommended for high performance of the proposed Tx coil, considering the four criteria in this paper.

As shown in Fig. 15, $M_{1,nom}$ decreases as N_m increases, whereas P_{c1} increases as N_m increases. Considering $U_{B,avg}$ and $B_{m,avg}$, as identified from Figs. 13 and 14, the normalized value of FoM in (13) can be found, as shown in Fig. 15. Therefore, it is found that the minimum point of the FoM is $N_m = 5$, which is the optimal point for the proposed IPT, according to the proposed design procedure. Note that N_m is always 5, regardless of l_c, e.g., 1.5 m $\times$ 1.5 m or 2.0 m $\times$ 2.0 m, so far as the shape of the Wi-power service area is square and d_a is half of l_1. If the shape of the Wi-power zone area is the others, e.g., circle, ellipse, and

TABLE I
LENGTH AND CURRENT VALUES OF THE PROPOSED DQ COILS

N_m	1	2	3	4	5	6	7	8	9
l_1 [mm]	80.0	32.0	20.0	15.0	11.5	9.5	8.0	7.0	6.0
I_{1d} $(= I_{1q})$ [A]	2.00	3.00	2.80	2.64	2.32	2.16	2.08	2.04	2.04

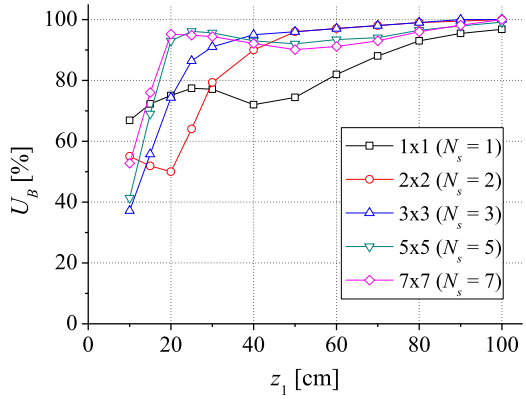

Fig. 13. Magnetic field uniformity U_B.

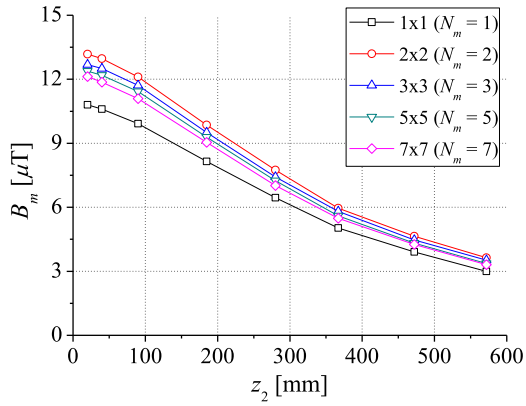

Fig. 14. Magnetic shielding effect B_m.

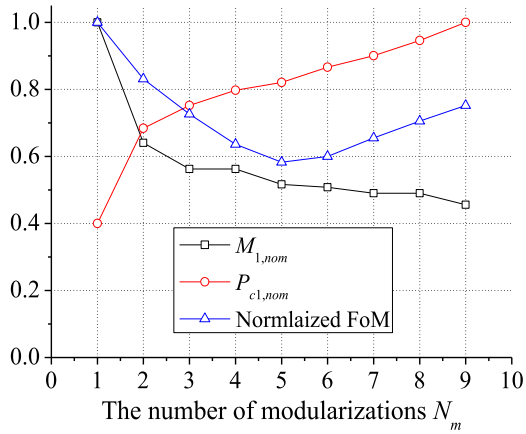

Fig. 15. Normalized FoM w.r.t. N_m.

rectangular, and d_a is changed, then the results may be different, which is not included in this paper due to limited pages.

To identify the rotating magnetic field, a FEM simulation by the ANSYS Maxwell simulation tool was performed, as shown in Fig. 16, where two orthogonal currents of i_{1d} and i_{1q} are driven through the DQ Tx coils and only the 1×1 and 5×5 cases are shown as representative examples. The polarities of the vector summation of the magnetic field $\boldsymbol{B}_t$ from (3) on the xy-plane are rotated for a switching period. For all the N_m cases, the rotating magnetic field is generated over 3-D space, and 3-D omnidirectional wireless powering, i.e., 6-DoF, is possible by the proposed modularized DQ Tx coils with a plane structure of the DQ Rx coils.

To identify the core loss reduction of the Tx core in accordance with the existence of the conductive plate, the magnetic field in the ferrite core for 5×5 modularization was simulated by a 3-D FEM simulation, as shown in Fig. 17. The magnetic field in the ferrite core can be significantly reduced by the conductive plate. As identified from Fig. 17, the averaged magnetic field inside the ferrite core for without and with the conductive plate cases are 23.0 mT and 16.6 mT, respectively; hence, 72% of the magnetic field reduction was achieved by the conductive plate in this application. The eddy current distribution on the conductive plate is shown in Fig. 18. The strong eddy current distribution was observed near the DQ dipole coil due to the strong magnetic field generated by the DQ dipole coil. The magnetic field distributions for $z_1 = 30$ cm and 70 cm, as an example, are shown in Fig. 19, where total summation of the magnetic field B_t is expressed on the xy-plane. As a result, 96.5% and 95.4% of the magnetic field uniformity were observed by simulation verification in Fig. 19, which corresponds to the simulation results of Fig. 13.

B. Static Circuit Analysis for DQ Currents Generation

To generate the rotating magnetic field over 3-D space, as identified from the previous section, 5×5 modularized DQ Tx coils with an aluminum plate having $l_c = 1$ m and $t_c = 1$ mm are installed, as shown in Fig. 20, where all the modularized DQ Tx coils are connected in series and drived by one DQ inverter. In Fig. 20, a series resonant capacitor is adopted in each Tx coil module so that the voltage stress of the resonant capacitors is mitigated by multiple segmented resonant capacitors, and a set of DQ Tx coils with a resonant capacitor is modularized for the DQ Tx module; hence, the proposed DQ Tx module, whose size is quite small enough to be a standard unit of the products, can be utilized to any size and shape of 3-D space. Assuming that all of the structures of the modularized DQ Tx coils including the number of winding turns are identical, the following conditions

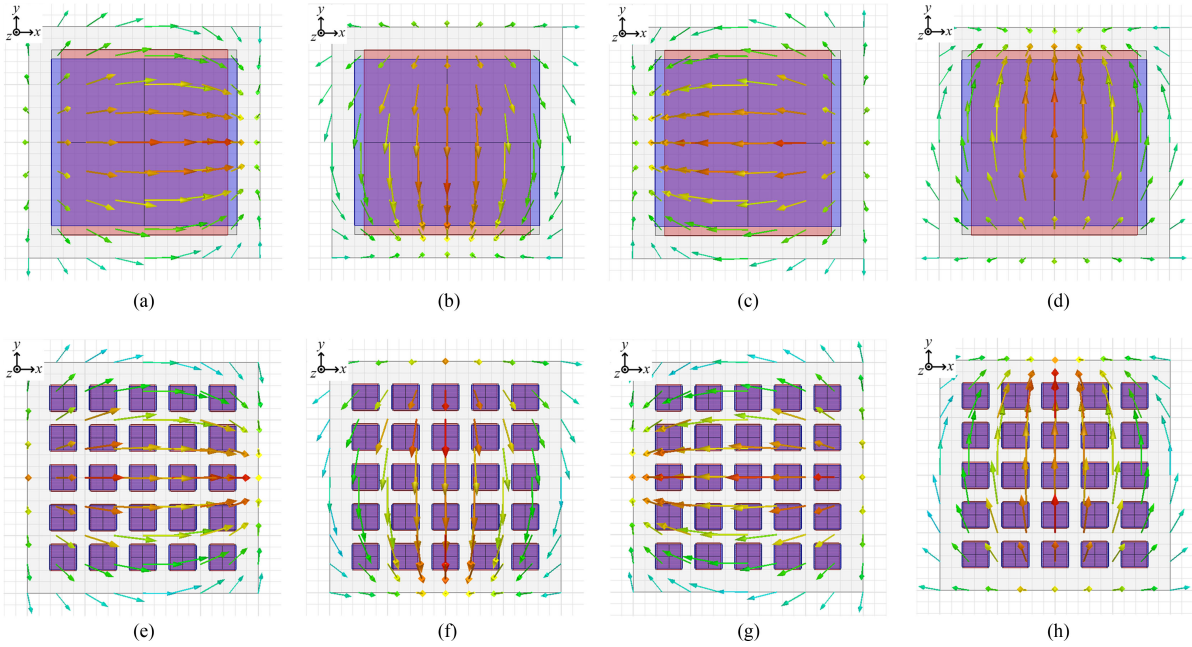

Fig. 16. FEM simulation of the proposed modularized DQ Tx coil with two orthogonal currents i_{1d} and i_{1q} at $z_1 = 0.5l_c$ for rotating magnetic field $\boldsymbol{B}_t$. (a) $\omega_s t = 0$ for 1×1 case. (b) $\omega_s t = \pi/2$ for 1×1 case. (c) $\omega_s t = \pi$ for 1×1 case. (d) $\omega_s t = 3\pi/2$ for 1×1 case. (e) $\omega_s t = 0$ for 5×5 case. (f) $\omega_s t = \pi/2$ for 5×5 case. (g) $\omega_s t = \pi$ for 5×5 case. (h) $\omega_s t = 3\pi/2$ for 5×5 case.

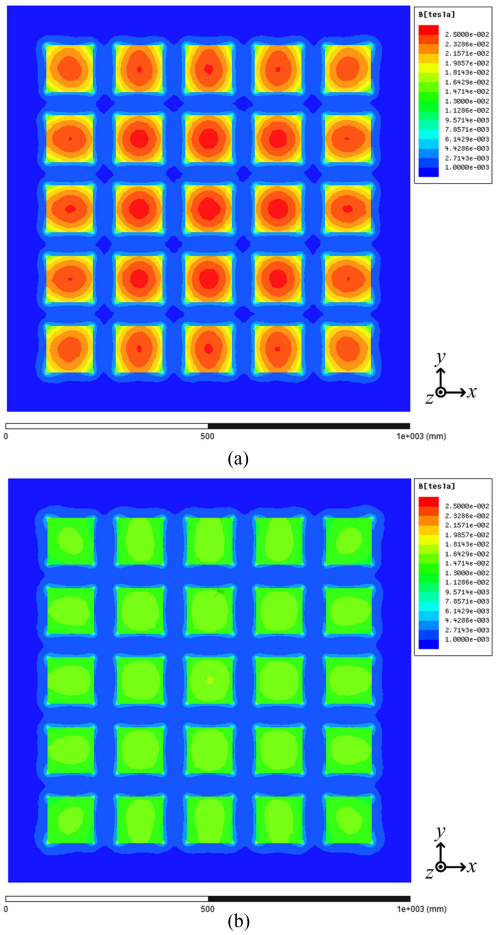

Fig. 17. FEM simulation results of the magnetic field in the Tx core for 5×5 modularization, where $I_{1d} = I_{1q} = 2.3$ A. (a) Without the conductive plate. (b) With the conductive plate.

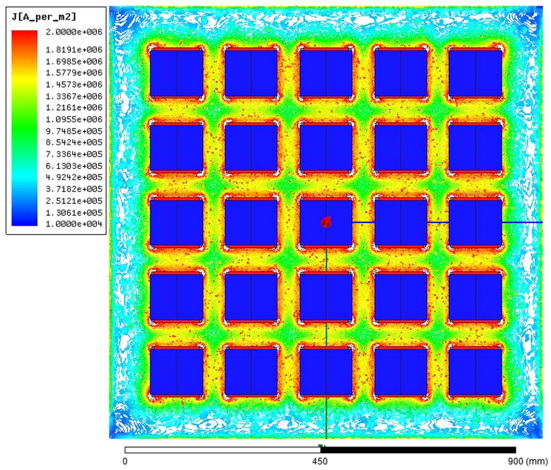

Fig. 18. FEM simulation results of the eddy current distribution on the conductive plate, where $I_{1d} = I_{1q} = 2.3$ A.

are then satisfied:

$$L_d = \sum_{k=1}^{N_m} L_{dk} = N_m L_{do} \quad \because L_{d1} = L_{d2} = \cdots = L_{dk} \equiv L_{do} \tag{14a}$$

$$\frac{1}{C_d} = \sum_{k=1}^{N_m} \frac{1}{C_{dk}} = \frac{N_m}{C_{do}} \quad \because C_{d1} = C_{d2} = \cdots = C_{dk} \equiv C_{do} \tag{14b}$$

$$\omega_{rdo} = \frac{1}{\sqrt{L_{d1}C_{d1}}} = \frac{1}{\sqrt{L_{d2}C_{d2}}} = \cdots = \frac{1}{\sqrt{L_{dk}C_{dk}}} = \frac{1}{\sqrt{L_{do}C_{do}}} \tag{14c}$$

where only the D-axis Tx coil is shown due to the symmetrical design of the DQ Tx coils in this section.

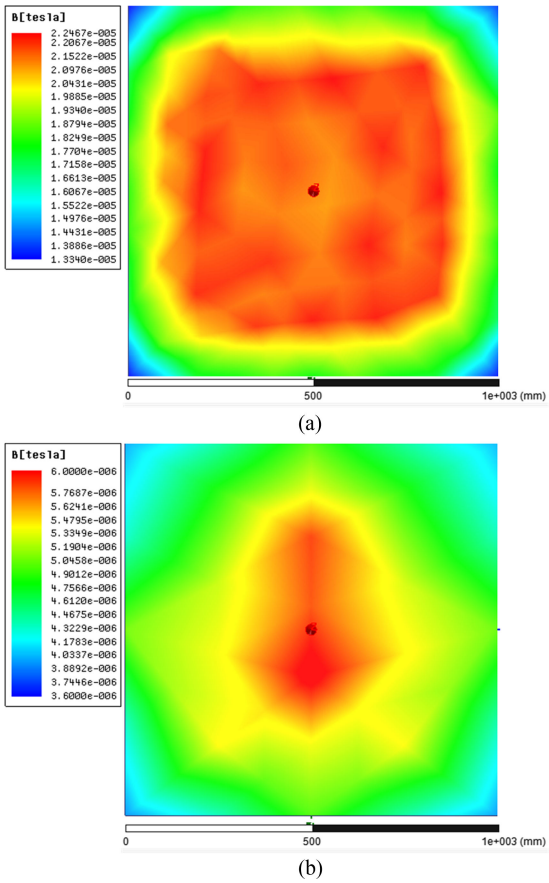

Fig. 19. FEM simulation results of the magnetic field distribution, where $I_{1d} = I_{1q} = 2.3$ A. (a) $z_1 = 30$ cm. (b) $z_1 = 70$ cm.

From (14), multiple DQ Tx coils composed of the Tx modules including DQ Tx coils and a series resonant capacitor can be connected in series and easily installed so that desirable 3-D space can be utilized for the proposed ubiquitous Wi-power zone. The electrical wiring connection for the D-axis Tx coil is illustrated in Fig. 21. Residual inductance may exist and will be appropriately resonated by an external resonant capacitor C_{dex} connected at the end of the line.

To provide DQ currents to the DQ Tx coils, a synchronized DQ inverter is adopted, as shown in Fig. 22, where it is assumed that magnetic coupling between the Tx and Rx coils can be neglected due to the extremely loosely coupled IPT in this paper. The input and the output of the proposed inverter are connected to a utility line with an ac–dc converter and DQ Tx coils, respectively. High-frequency switching legs $S_{d1}\&S_{d2}$ and $S_{q1}\&S_{d2}$ correspond to D- and Q-phase legs to generate DQ currents, respectively, and C_a and C_b are link capacitors

To generate DQ currents by the proposed DQ inverter, the following three conditions must be satisfied:

1) The magnitudes of each DQ current are the same ($I_d = I_q$).
2) The phase difference between DQ currents is $\pi/2$.
3) Zero-voltage-switching (ZVS) operation of the proposed inverter is guaranteed.

When the modularized DQ Tx coils are close to each other, the inductance may be changed due to the adjacent ferrite cores, which results in a change of the DQ currents and deviation of the ZVS conditions if the DQ Tx coils are directly connected to the inverter. In addition, when multiple Rx coils are placed nearby the Tx coil, the currents of the Tx coil may also vary. Therefore, it is necessary to generate constant DQ currents, regardless of surrounding environment and load variation conditions. For this remedy, additional *LC* filters $L_{df}\&C_{df}$ and $L_{qf}\&C_{qf}$ are adopted, as shown in Fig. 22. The phase difference of the gate signals between $v_{gs,d1}\&v_{gs,d2}$ and $v_{gs,q1}\&v_{gs,q2}$ is set to 90° for $\pi/2$ of the phase difference, and these *LC* filters are symmetrically designed for $I_d = I_q$.

The proposed DQ inverter in Fig. 22 can be represented, as shown in Fig. 23(a), where only the D-phase circuit is considered due to the symmetrical circuit design of the DQ phase legs, and the ESR of additional *LC* filters is neglected due to its small value. Assuming that only fundamental components of voltages and currents are considered and the duty cycle of the proposed inverter by $S_{d1}\&S_{d2}$ and $S_{q1}\&S_{q2}$ is 0.5 for simplicity of analysis, the output voltage of the proposed inverter V_{di} is determined as follows [35]–[37]:

$$V_{di} = \frac{2\sqrt{2}}{\pi} \cdot \frac{V_{dc}}{2} \cong 0.45 V_{dc}. \tag{15}$$

In Fig. 23(a), L_d is the total summation of the inductance for the Tx coils, as identified from (14a). Then, C_{de} and r_d are the total summation of the capacitance and resistance, respectively, as follows:

$$C_{de} = \frac{C_d C_{dex}}{C_d + C_{dex}} = \frac{C_{do} C_{dex}}{C_{do} + N_m C_{dex}} \tag{16a}$$

$$r_d = \sum_{k=1}^{N_m} r_{dk}. \tag{16b}$$

The output current of the proposed inverter I_{di} can be found by deriving the impedance Z_{di}, assuming that L_{df} and C_{df} are fully resonated, as follows:

$$|Z_{di}| \equiv \left| \frac{\boldsymbol{V}_{di}}{\boldsymbol{I}_{di}} \right| = \frac{\omega_s^2 L_{df}^2}{\left| j\omega_s \left(L_d - L_{df}\right) + \frac{1}{j\omega_s C_{de}} + r_d \right|}$$

$$= \frac{\omega_s^2 L_{df}^2}{\sqrt{\left\{\omega_s \left(L_d - L_{df}\right) - \frac{1}{\omega_s C_{de}}\right\}^2 + r_d^2}}$$

$$\left(\because j\omega_s L_{df} + \frac{1}{j\omega_s C_{df}} = 0\right) \tag{17a}$$

$$\therefore I_{di} = \frac{\sqrt{\left\{\omega_s \left(L_d - L_{df}\right) - \frac{1}{\omega_s C_{de}}\right\}^2 + r_d^2}}{\omega_s^2 L_{df}^2} V_{di}. \tag{17b}$$

By applying Norton's theorem to the left part of the circuit of Fig. 23(a), a simplified static circuit can be obtained, as shown in Fig. 23(b). A current source of I_{dn} to generate constant I_{1d}

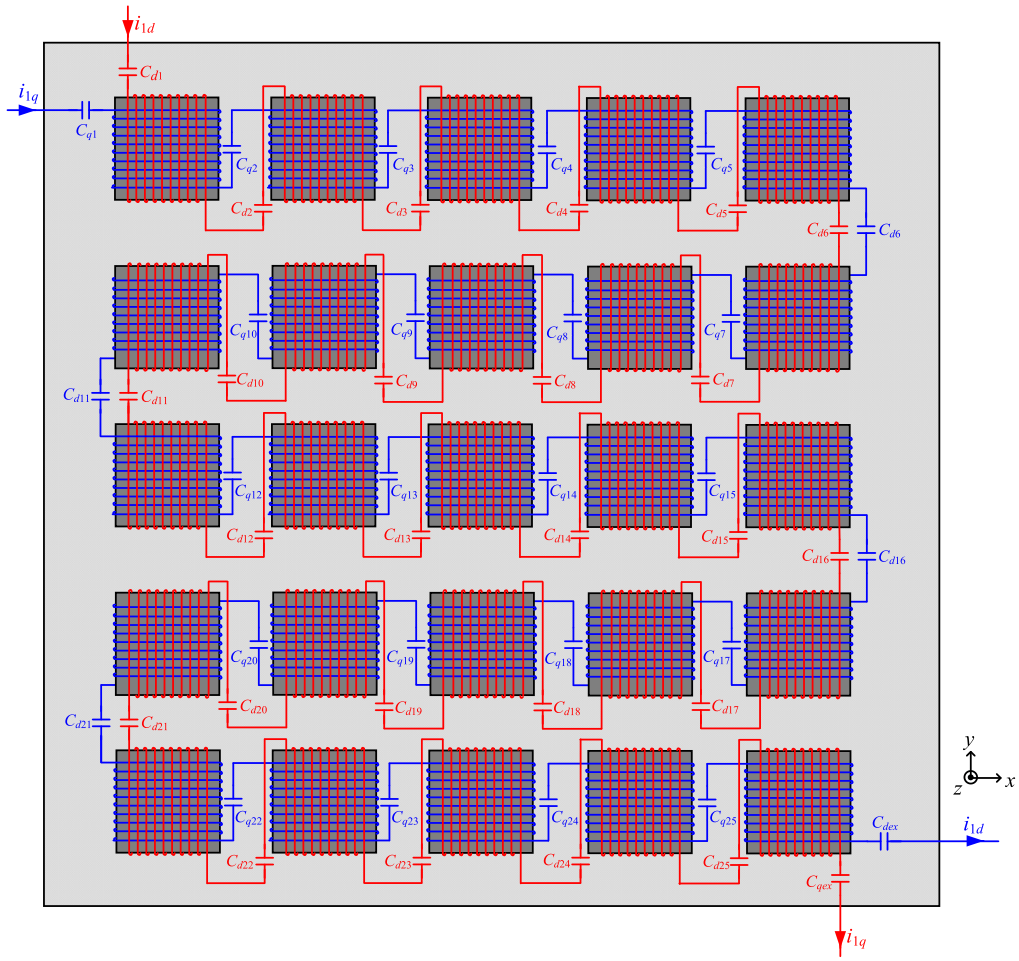

Fig. 20. Schematic of the proposed DQ coils for 5 × 5 modularization.

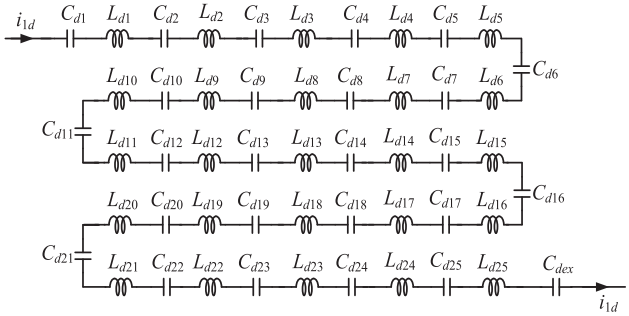

Fig. 21. Equivalent static circuit of the proposed D-axis coil for 5 × 5 modularization.

on the D-axis Tx coil in Fig. 23(b), regardless of load and inductance variations, can then be generated as follows:

$$\therefore I_{dn} = \frac{V_{di}}{\omega_s L_{df}} \cong \frac{0.45 V_{dc}}{\omega_s L_{df}} = I_{1d} \tag{18a}$$

$$|Z_{df}| = \left| \frac{j\omega_s L_{df}}{1-\omega_s^2 L_{df} C_{df}} \right| = \infty \quad \left(\because \omega_s = \frac{1}{\sqrt{L_{df} C_{df}}} \right). \tag{18b}$$

From (18a), DQ currents of the Tx coil are determined by L_{df} under the fixed switching frequency f_s and V_{dc}.

For reliable operation of the proposed inverter, the ZVS operations of the main switches $S_{d1}\&S_{d2}$ and $S_{q1}\&S_{q2}$ should be guaranteed; hence, the output impedance of the inverter Z_{di} should be inductive, the condition for which can be found from (17a) as follows:

$$j\omega_s (L_d - L_{df}) + \frac{1}{j\omega_s C_{de}} < 0 \ \rightarrow \therefore C_{de} < \frac{1}{\omega_s^2 (L_d - L_{df})}. \tag{19}$$

It is found from (19) that a smaller C_{de}, which can be modulated by C_{dex} in (16a), may be recommended for the ZVS condition under the fixed values of L_{df} and L_d. However, the smaller C_{de} causes a large I_{di}, as identified from (17b), which becomes a burden with regard to the current stress of the proposed inverter. Therefore, series resonant capacitances C_{dex} and C_{qex} for the DQ Tx coils should be appropriately selected, considering the ZVS condition of (19) and the current rating of switches $S_{d1}\&S_{d2}$ and $S_{q1}\&S_{q2}$ in (17b), which will be verified in Section IV.

IV. Experimental Verifications

A. Modularization of the Proposed IPT

To verify the characteristics of the magnetic shield, one-axis wound dipole coil with the conductive plate in

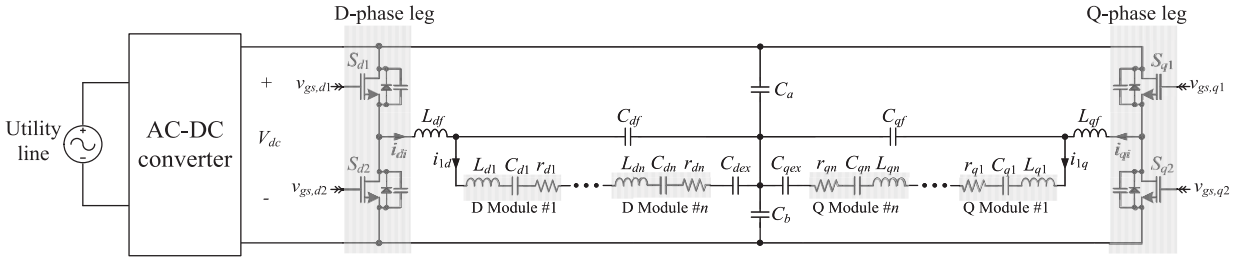

Fig. 22. Circuit configuration of the proposed DQ inverter connected to utility line and Tx coils.

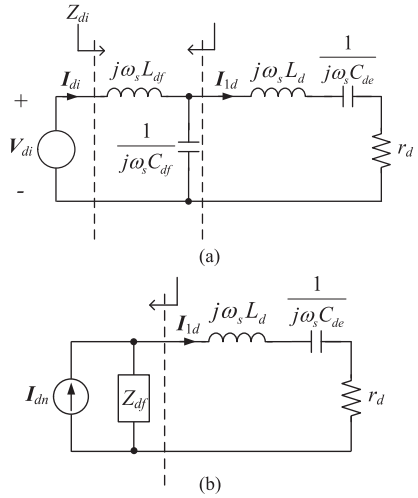

Fig. 23. Simplified final static circuit of the proposed DQ inverter for D-phase leg case. (a) Equivalent circuit of Fig. 22. (b) Norton equivalent circuit of (a).

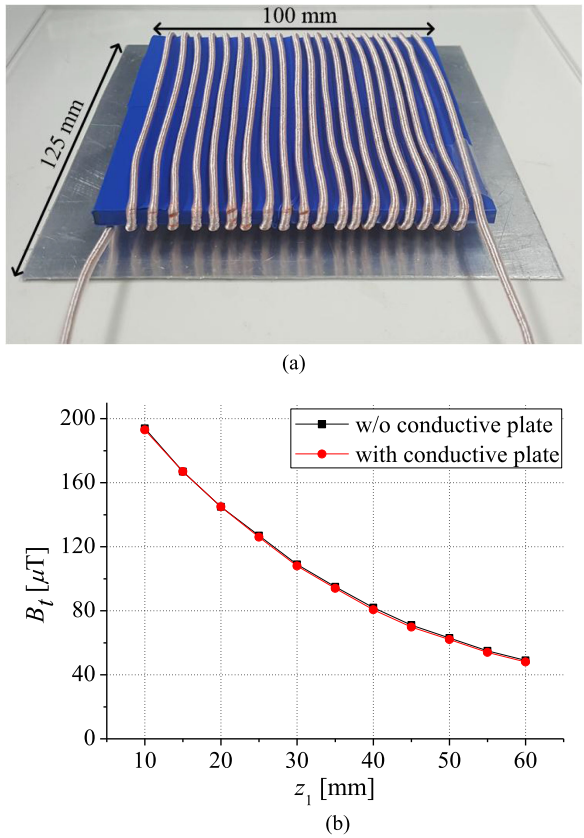

Fig. 24. Fabricated prototype of one-axis wound dipole coil and experimental results of the magnetic field. (a) Fabricated one-axis wound diploe coil with an aluminum plate. (b) Measured magnetic field w.r.t. z_1.

Fig. 4 was fabricated, as shown in Fig. 24(a). The parameter values for this dipole coil are the same as the parameters of the simulation verification, as described in Section II: $l_1 = 100$ mm, $l_c = 125$ mm, $I_1 = 1$ A, $N_1 = 20$ turns, $t_1 = 5$ mm, and $\mathrm{t_c} = 1$ mm. Self-inductance of one-axis wound dipole coil in Fig. 24 was measured as 43.29 μH and 63.37 μH for with and without the conductive plate cases, respectively. In addition, internal resistance for with and without the conductive plate cases were measured as 1.21 Ω and 1.67 Ω for with and without cases, respectively; hence, the losses of the dipole coil in Fig. 24 were measured as 1.21 W and 1.67 W when $I_1 = 1$ A for both with and without cases, respectively. From this experimental result, it can be found that total internal resistance including core loss, copper loss, and eddy loss with the conductive plate case becomes obviously decrease compared to without the conductive plate case, although the eddy loss is added for the conductive plate case, i.e., $r_1 > r_1{}' + r_{ce}$, as identified from Section II. Therefore, the conductive plate can improve the power efficiency under the same Tx coil current by reducing the core loss of the Tx coil. The measured magnetic field w.r.t. z_1 is shown in Fig. 24(b), where the experimental result matches well with the simulation result of Fig. 8. The magnetic field was measured by a magnetic field measurement device, i.e., SPECTRAN NF-5035 made by AARONIA AG. As shown in Fig. 24(b), little difference of the magnetic field was observed w.r.t. the existence of the conductive plate. Therefore, it is found that the conductive plate does not contribute the magnetic field forward front side, which corresponds to Wi-power zone, as identified from Fig. 8.

The analysis and design considerations of the proposed modularized IPT were verified by an experimental prototype of 5 × 5 modularized DQ Tx coils, as shown in Fig. 25(a), where the proposed IPT is composed of 25 Tx modules with variable capacitors. Aluminum was selected as the material of the conductive plate for the magnetic shielding, and the length and thickness of the conductive plate l_c and t_c were selected as 1 m and 1 mm, respectively; hence, a 1 m × 1 m × 0.7 m ubiquitous Wi-power zone is created as an example, as identified

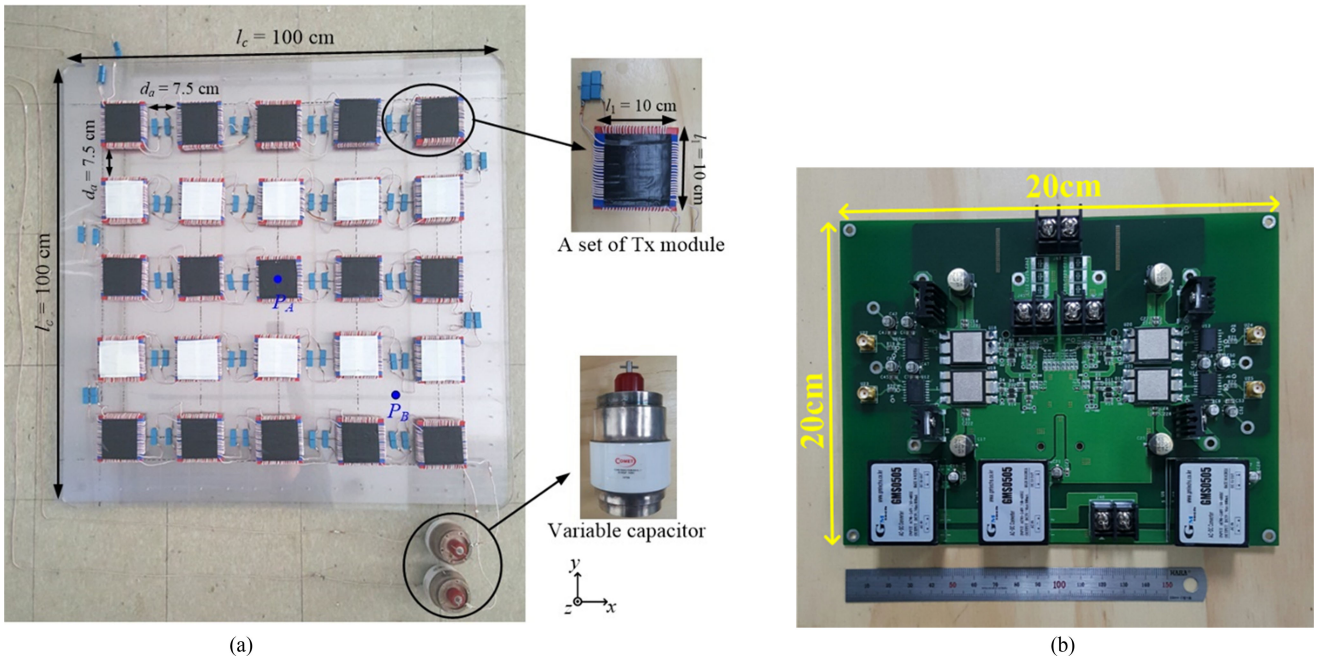

Fig. 25. Fabricated prototype of the proposed modularized DQ Tx coils for 5 × 5 modularization and DQ inverter. (a) Fabricated modularized DQ Tx coils with an aluminum plate. (b) Fabricated DQ inverter.

from Section III. The length of the ferrite core l_1 in Fig. 12 was selected as 10 cm, considering commercially available ferrite core in markets, and the material of the ferrite core adopted in this paper was PM12 from TODAISU. The thickness of the ferrite core t_1 was selected as 16 mm, considering the saturation of the core, and the diameter of the copper wire is 1.8 mm; hence, the total thickness of the proposed IPT including the aluminum plate is roughly 24 mm. The distance between DQ Tx coils d_a was selected as 7.5 cm and the gap between the aluminum plate and the proposed IPT d_c is 2 mm. The number of winding turns for DQ Tx coils N_d and N_q was selected as 20 turns: inductance for each DQ Tx module L_{do} and L_{qo} was measured as 69.5 μH and 70.6 μH, respectively. The switching frequency f_s was selected as 280 kHz, meeting the international guideline of Air-Fuel Alliance; hence, the capacitance in each resonant capacitor in a set of Tx module for DQ Tx coils C_{do} and C_{qo} in Fig. 25(a) was selected as 7.5 nF, considering commercially available components in markets. The residual inductance resonated by a number of modularized resonant capacitors was then resonated and modulated by C_{dex} and C_{qex} in Figs. 20–22, i.e., variable capacitors, as shown in Fig. 25(a), which can easily modulate the capacitance in a range of 50–500 pF manually. Therefore, by virtue of the multiple segmented resonant capacitors and the variable capacitors, voltage stress applied to the capacitors can be distributed and mitigated. The series quality factor of each DQ Tx module was calculated as 218.3 from $f_s = 280$ kHz, $L_{do} = 69.5$ μH, and $r_{do} = 0.56$ Ω. It is noteworthy that the quality factor of the proposed IPT comprising multiple Tx modules is almost constant as the number of Tx modules increases; hence, the ubiquitous Wi-power area can be extended by adding Tx modules without increment of the sensitivity of the proposed IPT. Note that color classification, i.e., black and white DQ Tx modules, implies different polarities of the DQ Tx coils for wire connection, as illustrated in Fig. 20 in detail. All parameter selections for the proposed Tx & Rx coils and the inverter are summarized in Table II.

TABLE II
PARAMETER SELECTIONS OF THE PROPOSED IPT

Parameters	Values	Parameters	Values	Parameters	Values
r_{do}	0.56 Ω	C_{df}, C_{qf}	26.9 nF	l_1	10 cm
r_{qo}	0.62 Ω	N_d, N_q	20	t_1	16 mm
L_{do}	69.5 μH	N_m	5	d_a	7.5 cm
L_{qo}	70.6 μH	l_c	100 cm	d_c	2 mm
L_{df}, L_{qf}	12.0 μH	t_c	1 mm	f_s	280 kHz
C_d, C_q	7.5 nF	l_{1t}	80 cm		

To generate constant DQ currents, a DQ inverter was fabricated, as shown in Fig. 25(b). L_{df} and L_{qf} in Figs. 22 and 23 for DQ Tx coils were selected as 12 μH in order to generate 2.3 A of constant DQ Tx currents I_{1d1} and I_{1q} at $V_{dc} = 110$ V in (18a): resonant capacitors for the additional LC filters C_{df} and C_{qf} were chosen as 26.9 nF for resonant condition of (17a). To verify the ZVS operations of the inverter, the experimental results as well as the simulation and calculation results are shown in Fig. 26. The output currents of the inverter for the DQ Tx coils I_{di} and I_{qi} in Fig. 26 can be changed by modulating C_{de} and C_{qe}, as identified from (17b), and ZVS operation of the proposed inverter can be found by the condition of (19). As shown in Fig. 26, if C_{de} and C_{qe} are too small, I_{di} and I_{qi} become too large, which significantly increases conduction loss of the inverter, although ZVS operation is satisfied. Therefore, appropriate values of C_{de} and C_{qe} should be chosen by easily tuning the variable capacitors: C_{de} and C_{qe} were selected

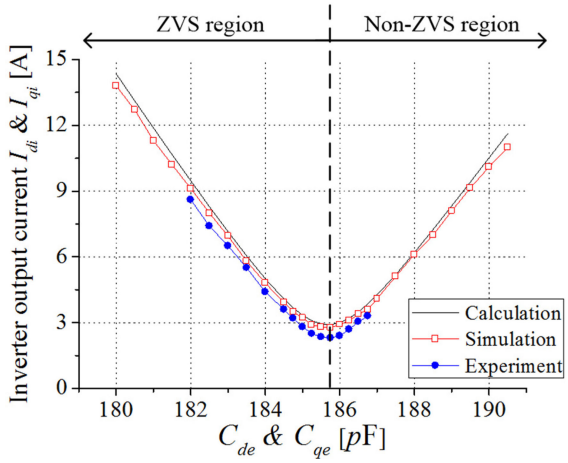

Fig. 26. Experimental results of i_{di} and i_{qi} w.r.t. C_{de} and C_{qe}, compared to calculation and simulation results for the ZVS operation of the proposed inverter.

as 185.5 pF for minimal ZVS currents in this paper. The discrepancy between calculation and experiment comes from harmonics and unexpected internal resistance, where calculation results consider only fundamental components of the voltages and currents. The operating waveforms of voltages and currents for the ZVS and DQ operations are shown in Fig. 27. In Fig. 27(a), $\pi/2$ phase difference for DQ currents was realized by $\pi/2$ phase difference of the gate signals between $v_{gs,d1}$&$v_{gs,d2}$ and $v_{gs,q1}$&$v_{gs,q2}$. As shown in Fig. 27(b), the output currents of the DQ inverter include harmonics, especially third and fifth components, due to the square-wave for the output voltages of the DQ inverter. In case of $C_{de} = C_{qe} = 185.5$ pF, as shown in Fig. 27(b), third and fifth harmonics were measured as 12.2% and 3.8%, whose values may not be significant for the ZVS operation of the inverter.

B. Magnetic Field Distribution

The magnetic field distribution of the proposed IPT for a wide-range ubiquitous Wi-power zone was verified to evaluate the magnetic field uniformity U_B, as shown in Figs. 28–30, where only $z_1 = 0.25l_c, 0.5l_c$, and $0.75l_c$ cases are described due to the page limit of this paper. The total summation of the magnetic field $\boldsymbol{B}_t$ is composed of the orthogonal vectors $\boldsymbol{B}_x, \boldsymbol{B}_y$, and $\boldsymbol{B}_z$, and its magnitude $B_t\ (= |\boldsymbol{B}_t|)$ can be determined by the principle of (4) [9], [24]. Note that the existence of the magnetic shield makes no difference for front side magnetic field distribution, which corresponds to ubiquitous Wi-power area, as identified from Figs. 8 and 24; hence, magnetic field measurement results for only magnetic shield case is included in this paper. As identified from Figs. 28–30, B_z is relatively large at the corner of the ubiquitous area, whereas B_x and B_y are dominant at the center of the ubiquitous area; hence, total summation of the magnetic field B_t can be evenly distributed. In general, when z_1 increases, the magnetic field area generated by B_x and B_y becomes large at the center and that generated

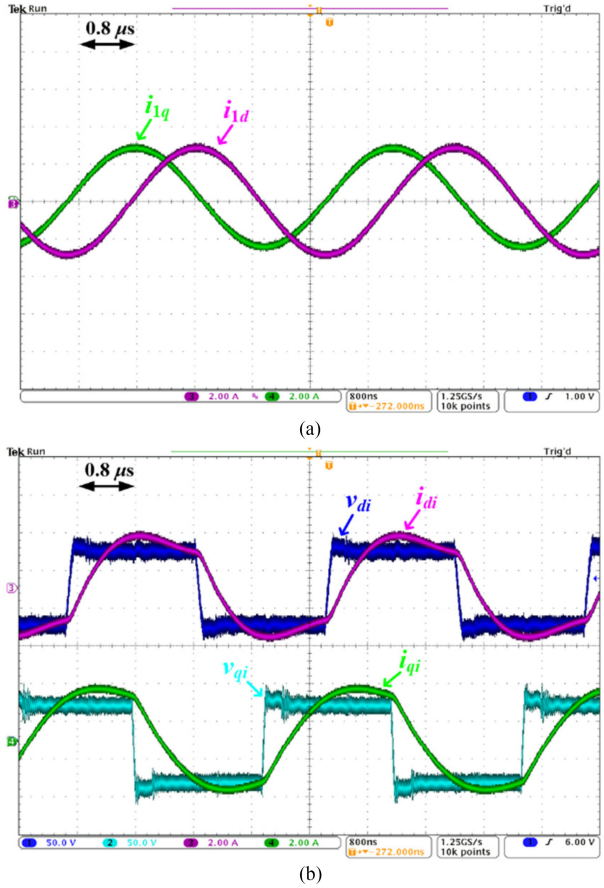

Fig. 27. Waveforms of voltages and currents for ZVS and DQ operations of the proposed inverter when $C_{de} = C_{qe} = 185.5$ pF. (a) DQ currents i_{1d} and i_{1q}. (b) DQ Inverter voltages and currents v_{di}, v_{di}, i_{di}, and i_{qi}.

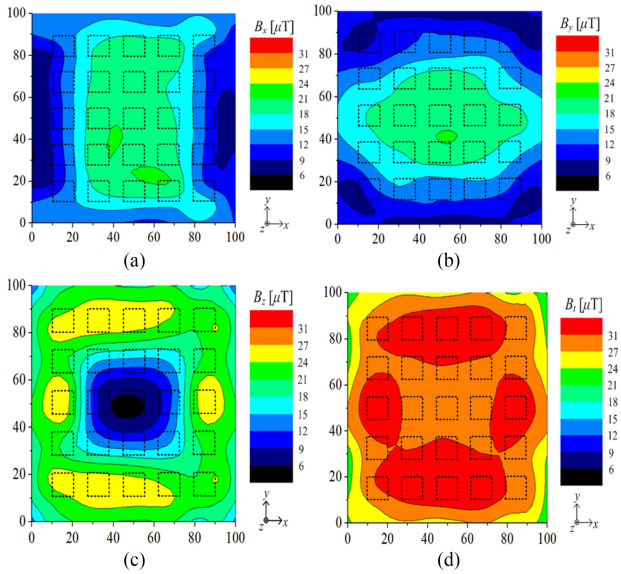

Fig. 28. Measured magnetic flux density at $z_1 = 0.25l_c = 25$ cm. (a) x-directional magnetic flux density $|\boldsymbol{B}_x|$. (b) y-directional magnetic flux density $|\boldsymbol{B}_y|$. (c) z-directional magnetic flux density $|\boldsymbol{B}_z|$. (d) Total summation of magnetic flux density $|\boldsymbol{B}_t|$.

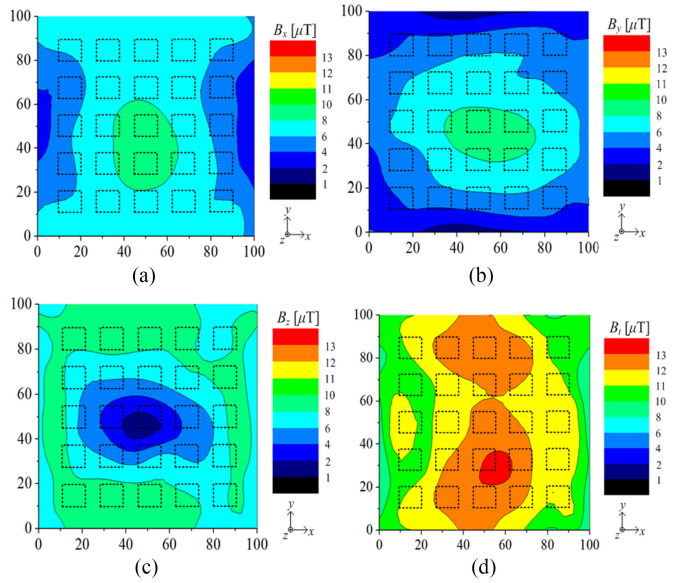

Fig. 29. Measured magnetic flux density at $z_1 = 0.5l_c = 50$ cm. (a) x-directional magnetic flux density $|\boldsymbol{B}_x|$. (b) y-directional magnetic flux density $|\boldsymbol{B}_y|$. (c) z-directional magnetic flux density $|\boldsymbol{B}_z|$. (d) Total summation of magnetic flux density $|\boldsymbol{B}_t|$.

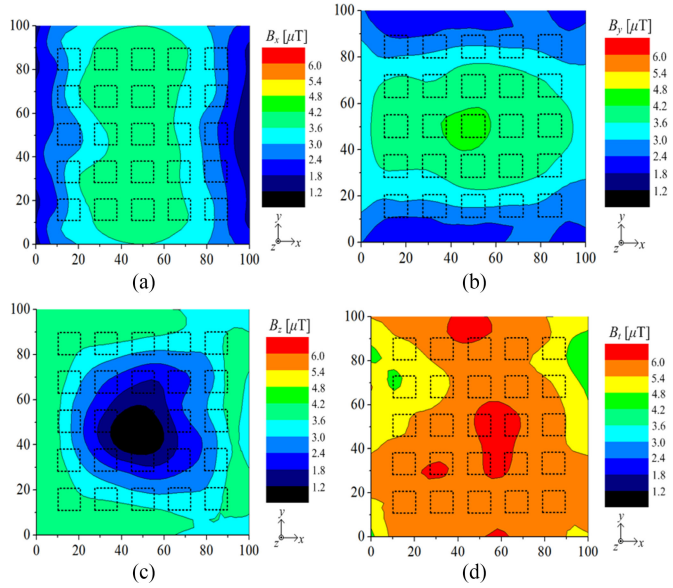

Fig. 30. Measured magnetic flux density at $z_1 = 0.75l_c = 75$ cm. (a) x-directional magnetic flux density $|\boldsymbol{B}_x|$. (b) y-directional magnetic flux density $|\boldsymbol{B}_y|$. (c) z-directional magnetic flux density $|\boldsymbol{B}_z|$. (d) Total summation of magnetic flux density $|\boldsymbol{B}_t|$.

by B_z becomes small at the corner. As a result, the uniformity of the magnetic field U_B for $z_1 = 0.25l_c, 0.5l_c,$, and $0.75l_c$ was measured as 95.5%, 92.1%, and 98.8%, respectively. These results are in good agreement with the simulation results of Fig. 13 and are superior to those of the conventional cross-dipole coil structure [9].

C. Three-Dimensional Omnidirectional Wireless Charging (6-DoF)

The 3-D omnidirectional wireless power characteristics, i.e., 6-DoF in this paper, were verified by the DQ Rx coil, as shown in Fig. 31. The Rx coil was fabricated similar with the DQ Tx coil: the length and thickness of the Rx coil are 10 cm and 4 mm, respectively, and the number of turns for horizontal and vertical windings is 20. As shown in Fig. 31, series resonant capacitors C_h and C_v were adopted to fully resonant reactance of L_h and L_v, and the values of lumped load resistors R_{hL} and R_{vL} were selected as the same values of r_h and r_v for maximum power delivery: $R_{hL} = r_h = 1.35\ \Omega$ and $R_{vL} = r_v = 1.41\ \Omega$. To easily rotate angles of Rx coils, three-axis rotational structure was used, as shown in Fig. 31.

To identify the free-positioning and 3-D omnidirectional wireless powering, load voltages of V_{hL} and V_{vL} for horizontal and vertical windings were measured w.r.t. different rotation angles of roll, pitch, and yaw $\theta_x, \theta_y,$, and θ_z for different z_1 of $0.25l_c, 0.5l_c$, and $0.75l_c$, as shown in Figs. 32–37. Due to the page limit and the similar characteristics of 3-D omnidirectional wireless power, only P_A and P_B in Fig. 25 were evaluated. As shown in Figs. 32 and 34, it can be found that B_x and B_y components of the magnetic field mostly occupy the P_A point, which is the center position of the ubiquitous area, whereas fewer components of B_z exist, as identified from Figs. 28–30. On the other hand, B_z becomes large at the P_B point, whose characteristics can be found in Figs. 35–37. As identified from Figs. 32–37, the null-voltage point does not exist for any positions or rotation angles. Therefore, either V_{hL} or V_{vL} is at least applied to load voltage V_L, which satisfies free-positioning wireless charging for any position and angle over a wide-range 3-D space.

D. Simultaneous Wireless Charging

To identify simultaneous wireless charging of the proposed IPT, nine DQ Rx coils were fabricated as an experimental verification example, as shown in Fig. 38, where all the Rx coils are identically fabricated. It is assumed that the positions of each Rx coil are far enough from adjacent Rx coils that wireless power receiving is not significantly affected, as shown in Fig. 38(a). If the distance between adjacent Rx coils becomes smaller, then the receiving load power in one of Rx coils may affect to the receiving load power in the other existing Rx coils, which may be not desirable to get high load power and power efficiency. The Rx circuit topology for the resonant capacitors and load resistors is the same as that of the DQ Rx coil used for 6-DoF, as described in Fig. 31. The distance between the Tx and Rx coils z_1 can be modulated by acrylic shelf and supporters, as shown in Fig. 38(b). As the number of Rx coils placed on the shelf increases, the total load power increases, as shown in Fig. 39, assuming that the arrangement of the Rx coils corresponds to Fig. 38(a). The center Rx coil, i.e., Rx5, receives large load power compared to the others, as shown in Fig. 39. The total load power for $z_1 = 30$ cm, 50 cm, and 70 cm was measured as 127.1 W, 38.2 W, and 14.2 W, respectively. The

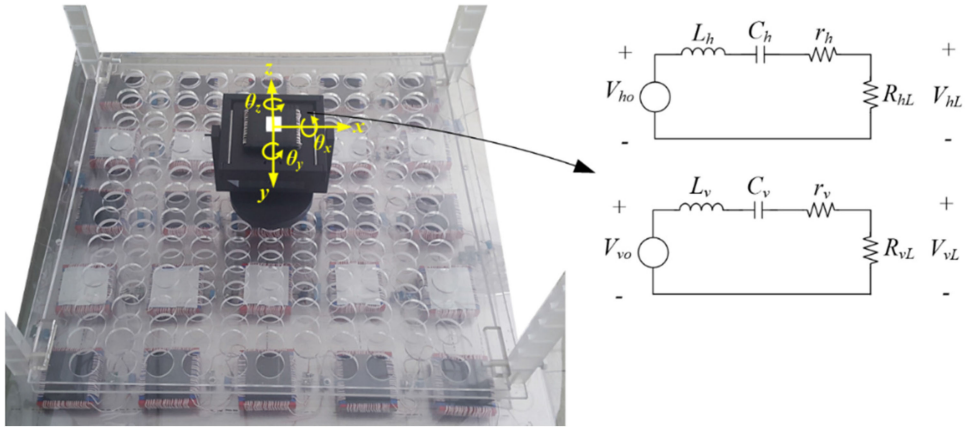

Fig. 31. Fabricated prototype of the DQ dipole Rx coil placed at P_A point and its equivalent circuit for horizontal and vertical wireless power receiving.

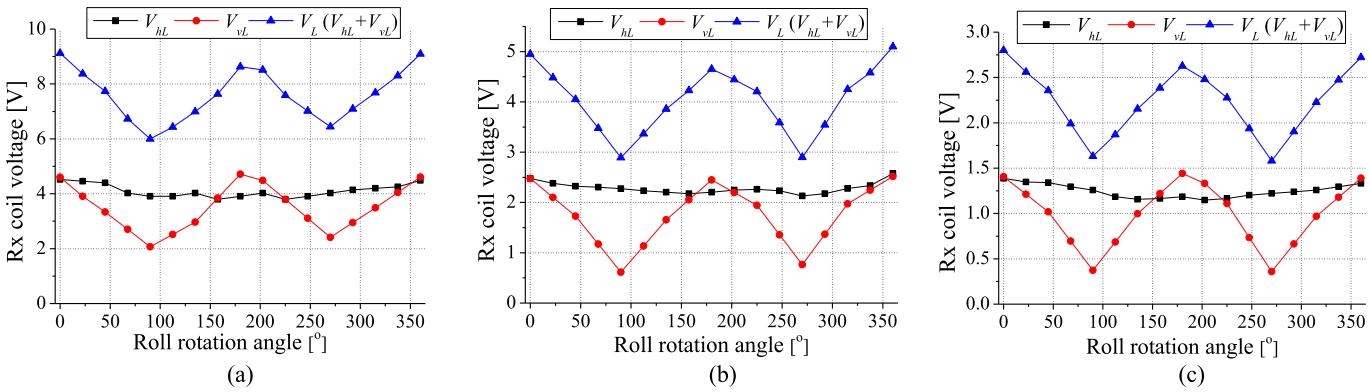

Fig. 32. Measured Rx coil voltages w.r.t. roll rotation angles θ_x for different z_1 at P_A point. (a) $z_1 = 0.25l_c = 25$ cm. (b) $z_1 = 0.5l_c = 50$ cm. (c) $z_1 = 0.75l_c = 75$ cm.

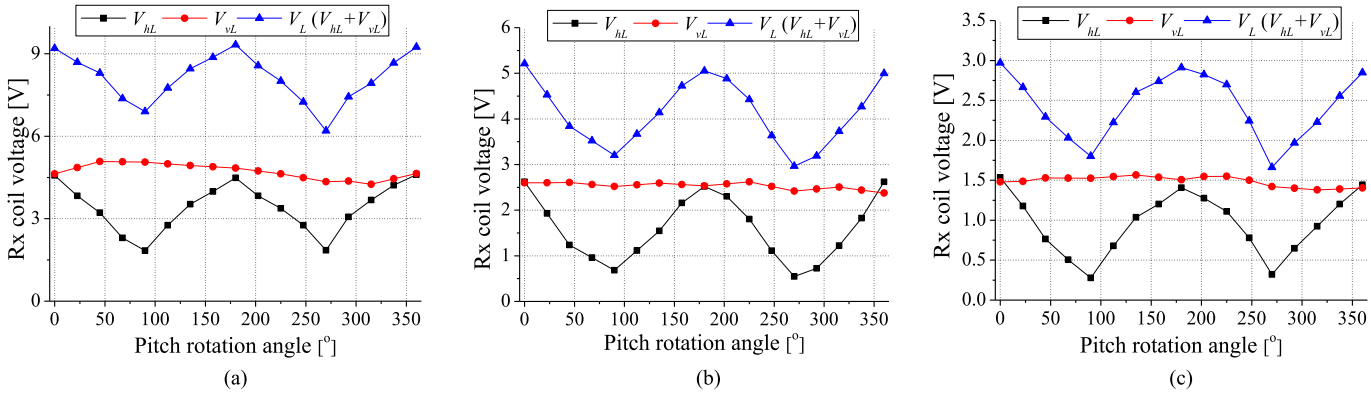

Fig. 33. Measured Rx coil voltages w.r.t. pitch rotation angles θ_y for different z_1 at P_A point. (a)$z_1 = 0.25l_c = 25$ cm. (b) $z_1 = 0.5l_c = 50$ cm. (c) $z_1 = 0.75l_c = 75$ cm.

surface temperature of the conductive plate after 10 min was measured as 27 °C under 23 °C of ambient room temperature by Ti10 FLUKE thermal camera.

To verify the effect of the conductive plate for highly efficient operation of the proposed IPT, the inductance of each DQ Tx module L_{do} and L_{qo} and the total ESR values of the proposed IPT for DQ Tx coils r_d and r_q were compared, as summarized in Table III. The results show that both the inductance and resistance decrease when the conductive plate is adopted, which corresponds to the results of the static analysis of the magnetic shielding, as identified from Section II. The power efficiencies for with and without the conductive plate cases were evaluated, as shown in Fig. 40, where the values of C_d and C_q are selected as 7.5 nF, as listed in Table II. When the total load power increases due to the increment of the number of Rx coils, the power efficiency increases. It is noteworthy that if the incre-

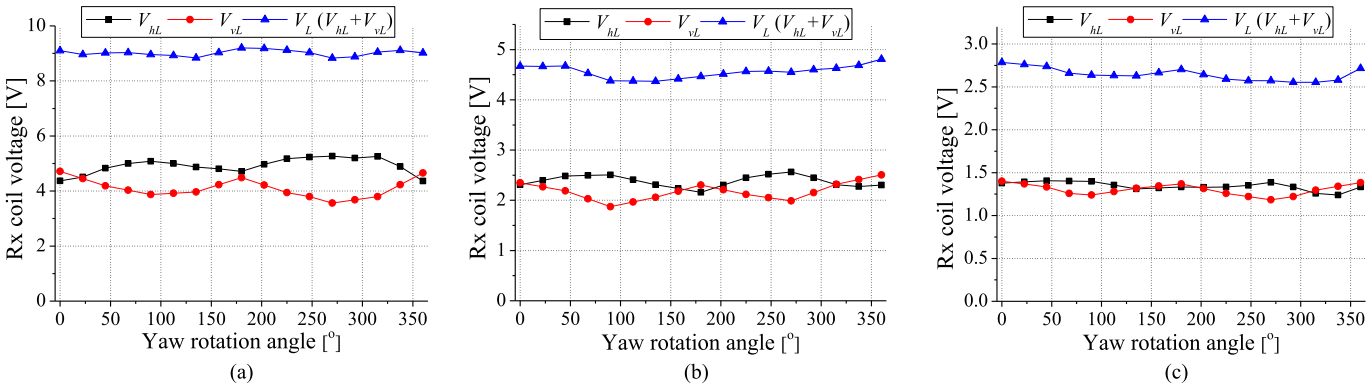

Fig. 34. Measured Rx coil voltages w.r.t. yaw rotation angles θ_z for different z_1 at P_A point. (a) $z_1 = 0.25l_c = 25$ cm. (b) $z_1 = 0.5l_c = 50$ cm. (c) $z_1 = 0.75l_c = 75$ cm.

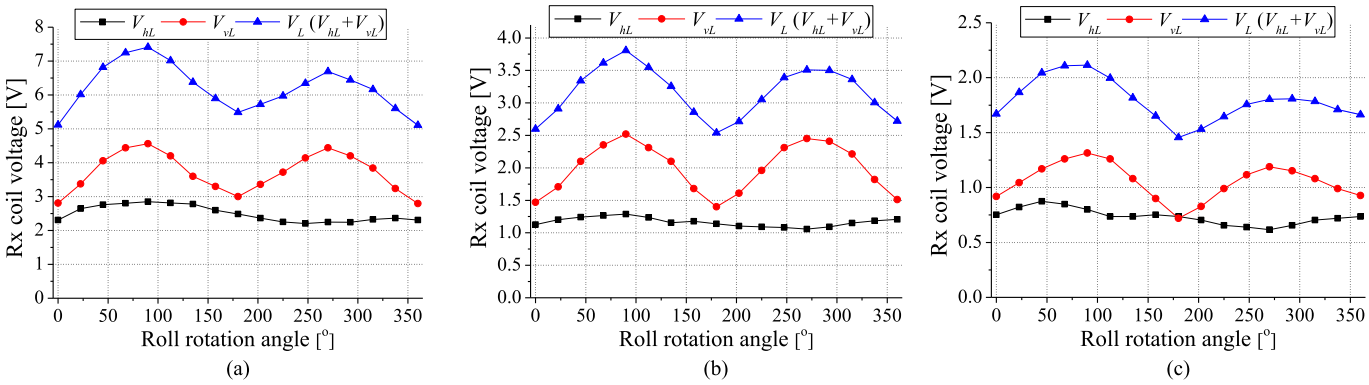

Fig. 35. Measured Rx coil voltages w.r.t. roll rotation angles θ_x for different z_1 at P_B point. (a) $z_1 = 0.25l_c = 25$ cm. (b) $z_1 = 0.5l_c = 50$ cm. (c) $z_1 = 0.75l_c = 75$ cm.

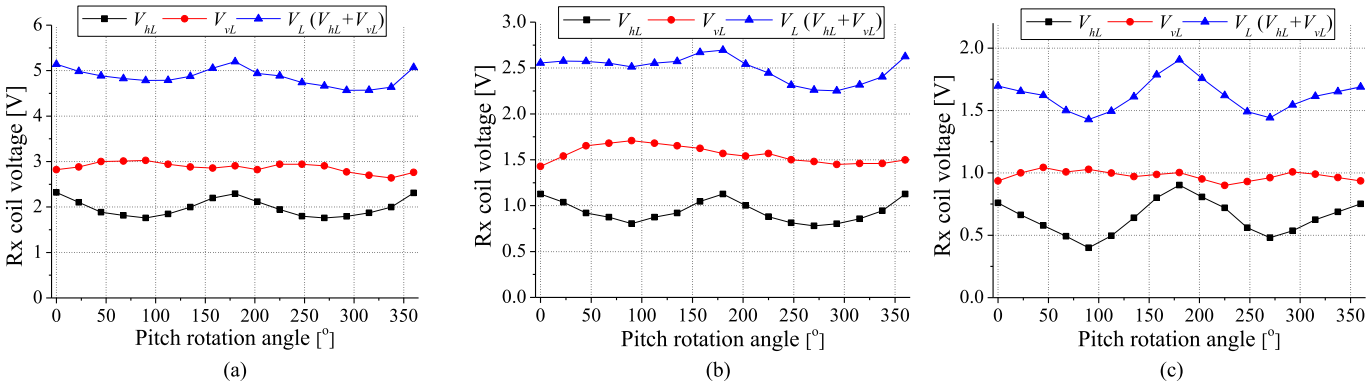

Fig. 36. Measured Rx coil voltages w.r.t. pitch rotation angles θ_y for different z_1 at P_B point. (a) $z_1 = 0.25l_c = 25$ cm. (b) $z_1 = 0.5l_c = 50$ cm. (c) $z_1 = 0.75l_c = 75$ cm.

ment of receiving load power is significantly high, e.g., Rx5, then the power efficiency also increases a lot. When 9 Rx coils were adopted, the measured power efficiencies of the conductive plate case for $z_1 = 30$ cm, 50 cm, and 70 cm were 36.8%, 19.2%, and 8.2%, respectively, whereas those without the conductive plate case were 31.0%, 14.9%, and 6.3%. The power loss analysis of the proposed IPT when $z_1 = 70$ cm is presented for both with and without the conductive plate cases, as shown in Fig. 41, where the parameter definitions are summarized in Table IV. In Fig. 41, all power losses can be analyzed by calculation, simulation, and experimental measurement. Core loss in the Tx coils P_{c1} can be calculated from (5), (6) based on simulated magnetic field of Fig. 17. Because P_{l2}, P_{inv}, and P_{co1} can be also calculated or measured, it is assumed that the rest

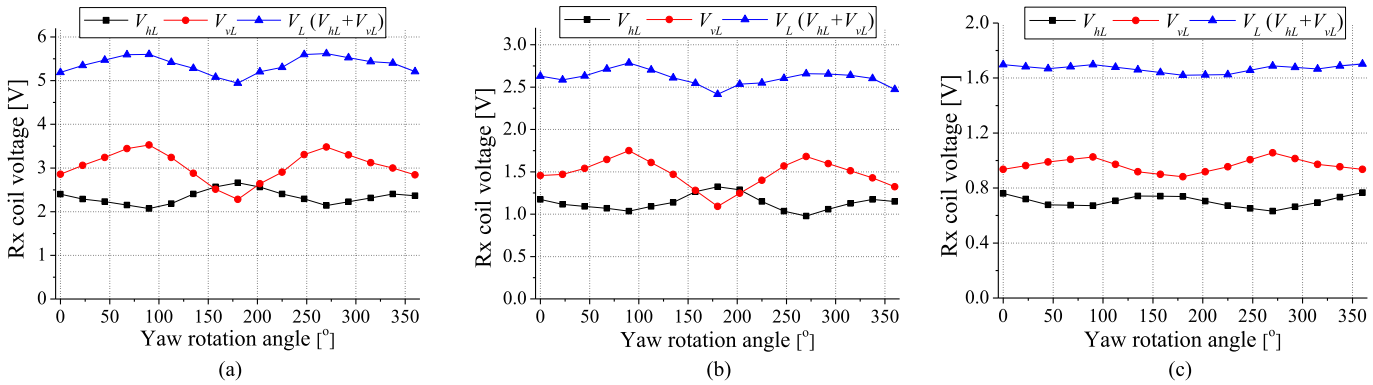

Fig. 37. Measured Rx coil voltages w.r.t. yaw rotation angles θ_z for different z_1 at P_B point. (a) $z_1 = 0.25l_c = 25$ cm. (b) $z_1 = 0.5l_c = 50$ cm. (c) $z_1 = 0.75l_c = 75$ cm.

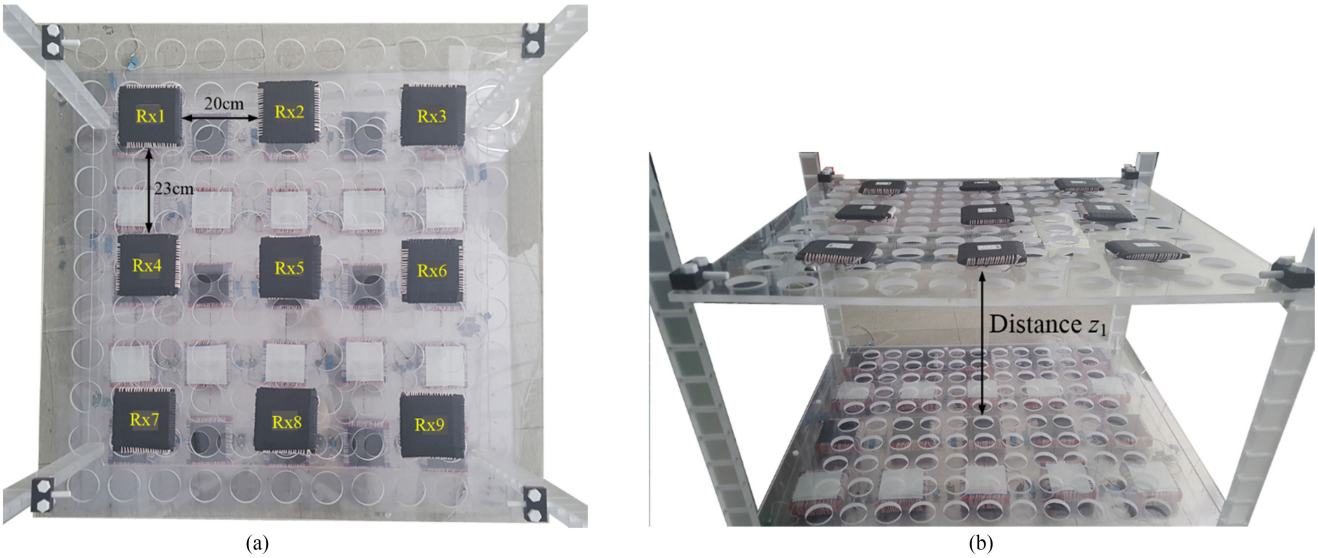

Fig. 38. Positions of the multiple Rx coils for load power and power efficiency. (a) Bird's view. (b) Side view.

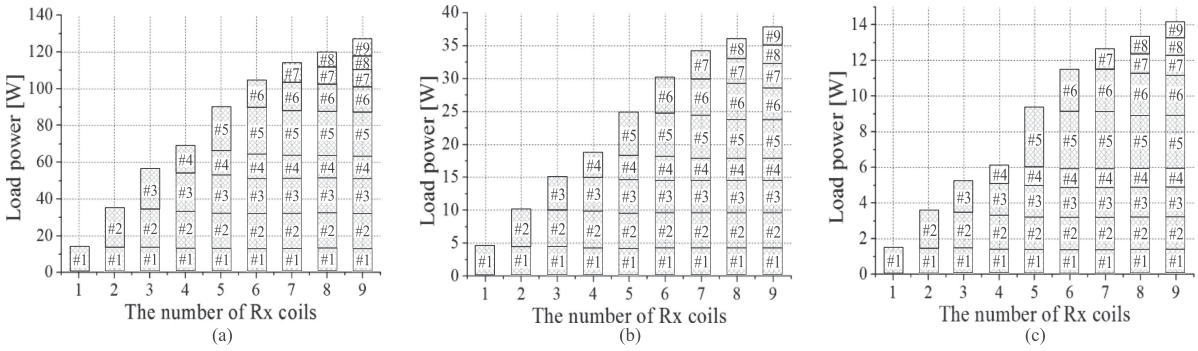

Fig. 39. Measured load power w.r.t. the number of Rx coils. (a) $z_1 = 30$ cm. (b) $z_1 = 50$ cm. (c) $z_1 = 70$ cm.

of power loss consumption comes from eddy loss of the conductive plate; as a result, it is found that 17.9% of the total losses is occupied by the eddy loss of the conductive plate. As shown in Fig. 41, the core losses per volume for without and with the conductive plate cases were calculated as 42.5 mW/cm^3 and 22.7 mW/cm^3, respectively. Considering the simulation results of Fig. 17, these estimated results for the core loss match well with the datasheet provided by PM12 from TODAISU. In Fig. 41, dominant loss are found to be P_{c1}, which occupies over a half of the total losses; hence, if a better ferrite core having low hysteresis and eddy losses is adopted for the DQ Tx core, the power efficiency will be improved for this application. From

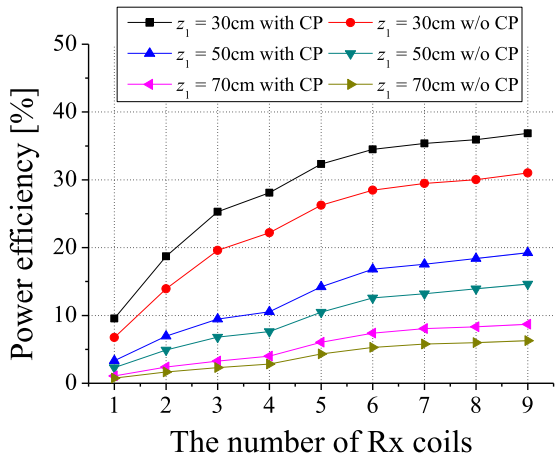

Fig. 40. Measured power efficiency w.r.t. the number of Rx coils, compared by the existence of the conductive plate, where $I_{1d} = I_{1q} = 2.3$ A.

TABLE III
COMPARISON OF MEASURED INDUCTANCE AND RESISTANCE W.R.T. THE EXISTENCE OF THE CONDUCTIVE PLATE

With conductive plate		Without conductive plate	
Parameters	Values	Parameters	Values
r_d	14.2 Ω	r_d	20.5 Ω
r_q	16.1 Ω	r_q	21.9 Ω
L_{do}	69.5 μH	L_{do}	93.4 μH
L_{qo}	70.6 μH	L_{qo}	101.2 μH

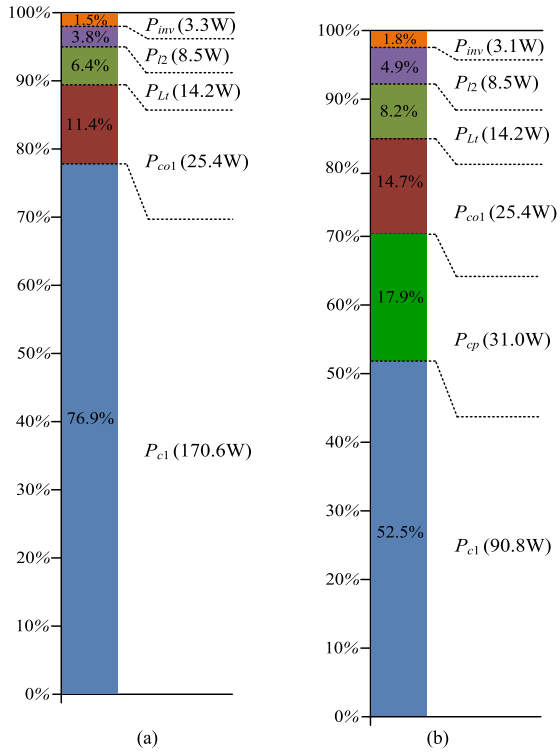

Fig. 41. Power loss analysis of the proposed IPT when $z_1 = 70$ cm, # of Rx coils = 9, and $I_{1d} = I_{1q} = 2.3$ A. (a) Without the conductive plate case. (b) With the conductive plate case.

TABLE IV
NOMENCLATURES FOR POWER LOSS ANALYSIS

Parameters	Remarks	Parameters	Remarks
P_{inv}	Conduction and switching losses in DQ inverter	P_{c1}	Core loss in the Tx coils
P_{l2}	Core and copper losses in Rx coils	P_{Lt}	Total load power
P_{co1}	Copper loss in the Tx coils	P_{cp}	Eddy loss in the conductive plate

these results, it is found that the conductive plate is recommended for highly efficient operation without affecting wireless load powering.

V. CONCLUSION

A simple and easily manufactured DQ Tx module-based ubiquitous Wi-power zone for 6-DoF wireless charging of an Rx coil and simultaneous wireless charging of Rx coils has been presented in this paper. Through the proposed optimum design procedure, the optimum number of modularizations for the DQ Tx modules was found by four design considerations for high magnetic field uniformity, high magnetic shield effect, low core loss, light weight, and cost-effectiveness. The prerequisite conditions for the proposed ubiquitous Wi-power zone were introduced and verified by a 5 × 5 modularized IPT for a 1 m × 1 m × 0.7 m ubiquitous Wi-power area. In this evenly distributed magnetic field environment created by the proposed IPT composed of the DQ Tx modules, free-positioning and 3-D omnidirectional wireless charging characteristics were satisfied over a wide-range of 3-D space. High magnetic field uniformity of 95.5%, 92.1%, and 98.8% for $z_1 = 25$ cm, 50 cm, and 75 cm, respectively, has been achieved; thus, meeting one of the crucial factors for a ubiquitous Wi-power zone. Simultaneous wireless charging of multiple Rx coils and the superiority of the conductive plate for high power efficiency have been verified by experiments: 8.2% power efficiency for the conductive plate case was achieved at $z_1 = 70$ cm, which is higher than 6.2% power efficiency for the case without the conductive plate. If the proposed DQ Tx module composed of the DQ Tx coils and series resonant capacitors becomes commercially available as a standard unit of the proposed IPT, a general wireless power solution for the proposed Wi-power zone over a wide-range 3-D space can be obtained. Therefore, any size and shape of installation places can be utilized for wireless power service areas by virtue of its simple Tx coil structure of the proposed Tx module.

REFERENCES

[1] S. E. Collier, "The emerging enernet: Convergence of the smart grid with the internet of things," *IEEE Ind. Appl. Mag.*, vol. 23, no. 2, pp. 12–16, Mar. 2017.
[2] J. A. Stankovic, "Research directions for the internet of things," *IEEE Internet Things J.*, vol. 1, no. 1, pp. 3–9, Feb. 2014.
[3] W. Rong *et al.*, "The internet of things (IoT) and transformation of the smart factory," in *Proc. Int. Electron. Symp.*, Sep. 2016, pp. 399–402.

[4] J. Robert *et al.*, "Micro-billing framework for IoT: Research & technological foundations," in *Proc. IEEE 4th Int. Conf. Future Internet Things Cloud*, Aug. 2016, pp. 301–308.
[5] M. W. Baker *et al.*, "Feedback analysis and design of RF power links for low-power bionic systems," *IEEE Trans. Biomed. Circuits Syst.*, vol. 1, no. 1, pp. 28–38, Mar. 2007.
[6] M. Stoopman *et al.*, "An RF-powered DLL-based 2.4-GHz transmitter for autonomous wireless sensor nodes," *IEEE Trans. Micro. Theory Techn.*, vol. 65, no. 7, pp. 2399–2408, Feb. 2017.
[7] N. Wang *et al.*, "One-to-multipoint laser remote power supply system for wireless sensor networks," *IEEE Sensors J.*, vol. 12, no. 2, pp. 389–396, Feb. 2012.
[8] J. Fakidis *et al.*, "Indoor optical wireless power transfer to small cells at nighttime," *J. Lightw. Technol.*, vol. 34, no. 13, pp. 3236–3258, Apr. 2016.
[9] Bo H. Choi *et al.*, "Six degrees of freedom mobile inductive power transfer by crossed dipole Tx and Rx coils," *IEEE Trans. Power Electron.*, vol. 31, no. 4, pp. 3252–3272, Apr. 2016.
[10] C. Park *et al.*, "Innovative 5m-off-distance inductive power transfer systems with optimum shaped dipole coils," *IEEE Trans. Power Electron.*, vol. 30, no. 2, pp. 817–827, Feb. 2015.
[11] B. H. Choi, V. X. Thai, E. S. Lee, J. H. Kim, and C. T. Rim, "Dipole-coil-based wide-range inductive power transfer systems for wireless sensors," *IEEE Trans. Ind. Electron.*, vol. 63, no. 5, pp. 3158–3167, Jan. 2016.
[12] Bo H. Choi *et al.*, "Development of highly reliable power and communication system for essential instruments under severe accidents in NPP," *Nuclear Eng. Technol.*, vol. 48, no. 5, pp. 1206–1218, Oct. 2016.
[13] J. H. Kim *et al.*, "Autonomous monitoring aerial robot system for nuclear power plants," in *Proc. Trans. Korean Nuclear Soc. Spring Meeting*, May 2016, pp. 30–31.
[14] T. Campi *et al.*, "Magnetic field levels in drones equipped with wireless power transfer technology," in *Proc. Asia-Pacific Int. Symp. Electromagn. Compat.*, May 2016, pp. 544–547.
[15] Su Y. Choi *et al.*, "Asymmetric coil sets for wireless stationary EV chargers with large lateral tolerance by Dominant field analysis," *IEEE Trans. Power Electron.*, vol. 29, no. 12, pp. 6406–6420, Dec. 2014.
[16] J. Huh *et al.*, "Narrow-width inductive power transfer system for On-Line Electrical Vehicles," *IEEE Trans. Power Electron.*, vol. 26, no. 12, pp. 3666–3679, Dec. 2011.
[17] S. Kim, G. Covic, and J. Boys, "Tripolar pad for inductive power transfer systems for EV Charging," *IEEE Trans. Power Electron.*, vol. 32, no. 7, pp. 5045–5057, Sep. 2016.
[18] D. Lin, C. Zhang, and S. Y. R. Hui, "Mathematic analysis of omnidirectional wireless power transfer—Part-II three-dimensional systems," *IEEE Trans. Power Electron.*, vol. 32, no. 1, pp. 613–624, Jan. 2017.
[19] C. Zhang, D. Lin, and S. Y. R. Hui, "Basic control principles of omnidirectional wireless power transfer," *IEEE Trans. Power Electron.*, vol. 31, no. 7, pp. 5215–5227, Sep. 2015.
[20] W. Ng, C. Zhang, D. Lin, and S. Hui, "Two- and three-dimensional omnidirectional wireless power transfer," *IEEE Trans. Power Electron.*, vol. 29, no. 9, pp. 4470–4474, Jan. 2014.
[21] H. Wu, G. Covic, J. Boys, and D. Robertson, "A series-tuned inductive-power-transfer pickup with a controllable AC-voltage output," *IEEE Trans. Power Electron.*, vol. 26, no. 1, pp. 98–109, Jan. 2011.
[22] C. K. Lee, W. X. Zhong, and S. Y. R. Hui, "Effects of magnetic coupling of nonadjacent resonators on wireless power transfer domino-resonator systems," *IEEE Trans. Power Electron.*, vol. 27, no. 4, pp. 1905–1916, Apr. 2012.
[23] B. H. Choi *et al.*, "Lumped impedance transformers for compact and robust coupled magnetic resonance systems," *IEEE Trans. Power Electron.*, vol. 30, no. 11, pp. 6046–6056, Nov. 2015.
[24] S. Y. Choi *et al.*, "Generalized active EMF cancel methods for wireless electric vehicles," *IEEE Trans. Power Electron.*, vol. 29, no. 11, pp. 5770–5783, Dec. 2013.
[25] E. Gati *et al.*, "Variable frequency controller for inductive power transfer in dynamic conditions," *IEEE Trans. Power Electron.*, vol. 32, no. 2, pp. 1684–1696, Apr. 2016.
[26] R. Zhou *et al.*, "An inductive power transfer system for driving multiple OLED light panels," *IEEE Trans. Power Electron.*, vol. 31, no. 10, pp. 7131–7147, Dec. 2015.
[27] D. T. Nguyen *et al.*, "Optimal shaped dipole-coil design and experimental verification of inductive power transfer system for home applications," in *Proc. IEEE Appl. Power Electron. Conf. Expo.*, Mar. 2016, pp. 1773–1779.
[28] Y. H. Sohn *et al.*, "Comparisons of magnetic field shaping methods for ubiquitous wireless power transfer," in *Proc. IEEE PELS Workshop Emerging Technol. Wireless Power*, Jun. 2015, pp. 1–6.
[29] Y. Du, H. Chen, and M. Chen, "Analysis of transient magnetic shielding made by conductive plates with a PEEC method," *IEEE Trans. Magn.*, vol. 53, no. 6, Feb. 2017, Art. no. 6300404.
[30] Y. Du, N. Xia, and M. Chen, "Joint modeling for conductive plates in low-frequency magnetic shielding," *IEEE Trans. Magn.*, vol. 49, no. 5, pp. 2005–2008, May 2013.
[31] K. Yamazaki *et al.*, "Open-type magnetically shielded room combined with square cylinders made of magnetic and conductive materials for MRIs," *IEEE Trans. Magn.*, vol. 44, no. 11, pp. 4183–4186, Dec. 2008.
[32] D.-H. Kim *et al.*, "Improved field localization in transcranial magnetic stimulation of the brain with the utilization of a conductive shield plate in the stimulator," *IEEE Trans. Bio. Eng.*, vol. 53, no. 4, pp. 720–725, Mar. 2006.
[33] A. Ayachit and M. K. Kazimierczuk, "Steinmetz equation for gapped magnetic cores," *IEEE Magn. Lett.*, vol. 7, Mar. 2016, Art. no. 1302704.
[34] J. Reinert *et al.*, "Calculation of losses in ferro- and ferrimagnetic materials based on the modified Steinmetz equation," *IEEE Trans. Ind. Appl.*, vol. 37, no. 4, pp. 1055–1061, Aug. 2002.
[35] E. S. Lee *et al.*, "Temperature-robust LC^3 passive LED drivers with low THD, high efficiency and PF, and long life," *IEEE J. Emerging Sel. Topics Power Electron.*, vol. 3, no. 3, pp. 829–840, Sep. 2015.
[36] C. T. Rim, D. Y. Hu, and G. H. Cho, "Transformers as equivalent circuits for switches: general proofs and D-Q transformation-based analysis," *IEEE Trans. Ind. Appl.*, vol. 26, no. 4, pp. 777–785, Jul./Aug. 1990.
[37] C. T. Rim, "Unified general phasor transformation for AC converters," *IEEE Trans. Power Electron.*, vol. 26, no. 9, pp. 2465–2475, Sep. 2011.

Eun S. Lee (S'13) was born in Korea in 1986. He received the B.S. degree in electrical engineering from Inha University, Incheon, South Korea, in 2012, and the M.S. and Ph.D. degrees in nuclear and quantum engineering from the Korea Advanced Institute of Science and Technology, Daejeon, South Korea, in 2014 and 2017, respectively.

His current research interests include the field of power converters, LED drivers, and wireless power transfer systems.

Yeung H. Sohn (S'14) was born in Korea, in 1990. He received the B.S., M.S., and Ph.D. degrees in electrical engineering all from the Korea Advanced Institute of Science and Technology (KAIST), Daejeon, South Korea, in 2012, 2014, and 2018, respectively.

His research interests include a highly reliable design of an ultrahigh power dc–ac conversion systems for the inductively coupled plasma and developing a graphical analysis method for the high-order circuit networks in the inductive power transfer system.

Byeong G. Choi (S'15) was born in Korea in 1990. He received the B.S. degree in mechanical engineering from Pusan National University, Busan, South Korea, in 2015. He is currently working toward the integrated Master's Ph.D. degree in electrical engineering at Korea Advanced Institute of Science and Technology, Daejeon, South Korea.

His current research interests include the field of power converters and wireless power transfer systems.

Seung H. Han (S'14–M'16) was born in Korea in 1970. He received the B.S. and M.S. degrees in electrical engineering all from Korea Advanced Institute of Science and Technology (KAIST), Daejeon, South Korea, in 1998, and 2000, respectively.

Since 2014, he has been a CEO & CTO of Teslas Co., Ltd. He has been developing various wireless power technologies and products. From 2009 to 2014, he was a CTO of DE Electron Co., Ltd, where he has developed various power electronics products including LED drivers for LCD TV, dimming systems for LED lighting, etc.

Chun T. Rim (M'90–SM'11) received the B.S. (Hons.) degree in electrical engineering from the Kumoh Institute of Technology, Gumi, South Korea, in 1985, and the M.S. and Ph.D. degrees in electrical engineering from the Korea Advanced Institute of Science and Technology (KAIST), Daejeon, South Korea, in 1987 and 1990, respectively.

From 2007 to 2016, he was an Associate Professor with KAIST. He is currently a Full Professor with the Gwangju Institute of Science and Technology, South Korea. He has authored or coauthored 160 technical papers, written 14 books, and holds 150 patents (awarded and pending).

Dr. Rim received numerous awards, including the Best Paper Award of IEEE TRANSACTIONS ON POWER ELECTRONICS (TPEL) in 2015 and IEEE JOURNAL OF EMERGING AND SELECTED TOPICS IN POWER ELECTRONICS in 2016 both in wireless power transfer (WPT). He is currently an Associate Editor of IEEE TPEL and the J-ESTPE, a Guest Editor of the Special Issue on WPT of the IEEE TPEL, IEEE TRANSACTIONS ON INDUSTRIAL ELECTRONICS, and J-ESTPE, and the General Chair of the 2015 and 2016 IEEE Workshop on Wireless power.